

The Herschel-HIFI view of mid-IR quiet massive protostellar objects[★]

F. Herpin,^{1,2} L. Chavarría^{1,2,3}, T. Jacq^{1,2}, J. Braine^{1,2}, F. van der Tak⁴, F. Wyrowski⁵, E. F. van Dishoeck^{6,7}, A. Baudry^{1,2}, S. Bontemps^{1,2}, L. Kristensen⁸, M. Schmalzl⁶, and J. Mata¹

¹ Univ. Bordeaux, LAB, UMR 5804, F-33270, Floirac, France.

² CNRS, LAB, UMR 5804, F-33270, Floirac, France, e-mail: herpin@obs.u-bordeaux1.fr

³ CONICYT-Universidad de Chile, Camino del Observatorio 1515, Santiago, Chile.

⁴ SRON Netherlands Institute for Space Research, PO Box 800, 9700AV, Groningen, The Netherlands

⁵ Max-Planck-Institut für Radioastronomie, Auf dem Hügel 69, 53121 Bonn, Germany

⁶ Leiden Observatory, Leiden University, PO Box 9513, 2300 RA, Leiden, The Netherlands

⁷ Max Planck Institut für Extraterrestrische Physik, Giessenbachstrasse 1, 85748 Garching, Germany

⁸ Harvard-Smithsonian Center for Astrophysics, 60 Garden Street, Cambridge, MA 02138, USA

Received; accepted

ABSTRACT

Aims. We present Herschel/HIFI observations of 14 water lines in a small sample of galactic massive protostellar objects: NGC6334I(N), DR21(OH), IRAS16272-4837, and IRAS05358+3543. Using water as a tracer of the structure and kinematics, we aim to individually study each of these objects, to estimate the amount of water around them, but to also shed light on the high-mass star formation process.

Methods. We analyze the gas dynamics from the line profiles using Herschel-HIFI observations acquired as part of the WISH key-project of 14 far-IR water lines (H_2^{16}O , H_2^{17}O , H_2^{18}O), and several other species. Then through modeling of the observations using the RATRAN radiative transfer code, we estimate outflow, infall, turbulent velocities, molecular abundances, and investigate any correlation with the evolutionary status of each source.

Results. The four sources (plus previously studied W43-MM1) have been ordered in terms of evolution based on their SED: NGC6334I(N) \rightarrow W43-MM1 \rightarrow DR21(OH) \rightarrow IRAS16272-4837 \rightarrow IRAS05358+3543. The molecular line profiles exhibit a broad component coming from the shocks along the cavity walls associated with the protostars, and an infalling (or expansion for IRAS05358+3543) and passively heated envelope component, with highly supersonic turbulence likely increasing with the distance from the center. Accretion rates between 6.3×10^{-5} and $5.6 \times 10^{-4} \text{ M}_{\odot} \text{ yr}^{-1}$ are derived from the infall observed in three of our sources. The outer water abundance is estimated to be at the typical value of a few 10^{-8} while the inner abundance varies from 1.7×10^{-6} to 1.4×10^{-4} with respect to H_2 depending on the source.

Conclusions. We confirm that regions of massive star formation are highly turbulent and that the turbulence likely increases in the envelope with the distance to the star. The inner abundances are lower than the expected 10^{-4} perhaps because our observed lines do not probe deep enough into the inner envelope, or because photodissociation through protostellar UV photons is more efficient than expected. We show that the higher the infall/expansion velocity in the protostellar envelope, the higher is the inner abundance, maybe indicating that larger infall/expansion velocities generate shocks that will sputter water from the ice mantles of dust grains in the inner region. High-velocity water must be formed in the gas-phase from shocked material.

Key words. ISM: molecules – ISM: abundances – Stars: formation – Stars: protostars – Stars: early-type – Line: water profiles

1. Introduction

The importance of high-mass stars ($M > 8 \text{ M}_{\odot}$) in the matter cycle in the Universe and the evolution of galaxies is well known (e.g. Zinnecker & Yorke 2007; Tan et al. 2014). As powerful sources of UV and driving strong outflows they deeply influence their environment. Despite this fundamental role, their formation is still not well understood due to their rareness, often large distances and embeddedness.

Empirically, high-mass star formation may be divided into several stages (e.g. van der Tak et al. 2000; Beuther et al. 2007; Mottram et al. 2011) leading to the (not unique) following evolutionary sequence: from the initial stage massive pre-stellar

cores (PSC's), to high-mass protostellar objects (HMPO's), hot molecular cores (HMC's), and finally to the more evolved ultra-compact HII regions (UCHII). While pre-stellar cores represent a quiet phase with no significant luminosity (Ragan et al. 2012) or activity (infall, outflow, or maser activity, Shipman et al. 2014), the HMPO stage is characterized by the presence of an active protostar exhibiting infall of a massive envelope onto the central star and strong outflows. Then, the temperature of the inner regions of the protostellar envelope will increase, going beyond the evaporation limits of molecules on the grains, hence enriching the envelope with complex molecules leading to the formation of a HMC. Later when the star gets hot enough to emit significant Lyman continuum, it will ionize the surrounding gas, leading to the formation of an UCHII. Based on the definition of Motte et al. (2007), HMPO sources can be divided in two different types depending on their $21 \mu\text{m}$ flux: the mid-IR-quiet

[★] Herschel is an ESA space observatory with science instruments provided by European-led Principal Investigator consortia and with important participation from NASA.

Table 1. Source list and parameters

Object	RA	Dec ^a	d ^a	V_{LSR}^a	L_{bol}^a	M_{env}^a	F_{12}^b	F_{21}^b	$L^{0.6}M_{env}^{-1}$	λ_{Fmax}	F_{35}/F_{total}^c
	[h m s]	[° ' "]	[kpc]	[km s ⁻¹]	[10 ³ L _⊙]	[M _⊙]	[Jy]	[Jy]		[μm]	
NGC6334I(N)	17 20 55.2	-35 45 04.1	1.7	-3.3	1.9	3826	0.0	0.6	0.02	220.6	0.7
W43-MM1	18 47 47.0	-01 54 28.0	5.5	+98.8	23	7550	0.0	0.7	0.05	131.7	0.5
DR21(OH)	20 39 00.8	+42 22 48.0	1.5	-3.1	13	472	0.3	1.3	0.6	100.0	1.7
IRAS16272-4837	16 30 58.7	-48 43 55.0	3.4	-46.2	24	2170	0.5	11.6	0.2	108.0	3.5
IRAS05358+3543	05 39 13.1	+35 45 50.0	1.8	-17.6	6.3	142	0.2	17.2	1.4	81.1	7.7

Notes. ^(a) Taken from van der Tak et al. (2013) based on JCMT/SCUBA and APEX/LABOCA data. ^(b) The F_{12} and F_{21} are the MSX values for the 12 and 21 μm flux density (or values estimated from the SED fitting for W43-MM1 and NGC6334I(N)), corrected for the distance to each source ($F_{\lambda} \times (d/1.5\text{kpc})^2$). ^(c) F_{35}/F_{total} is the ratio of the integrated flux over the range 0-35 microns and the total integrated flux.

dense cores ($F_{21} < 10$ Jy) and the more evolved mid-IR bright ones ($F_{21} > 10$ Jy). The distinction of mid-IR quiet and bright being different evolutionary stages is not obvious since geometry plays a significant role, and this still uncertain scenario may evolve and be constrained, e.g. by further observations. In this paper, the mid-IR quiet HMPOs will be studied.

The "classical" issue in massive star formation about how the accretion of matter can overcome radiative pressure is now well addressed by models considering a protostar-disk system (e.g., Yorke & Sonnhalter 2002; Krumholz et al. 2005; Banerjee & Pudritz 2007). More recently, the last generation simulations of Kuiper et al. (2010, 2015) demonstrate that disk accretion and protostellar outflows enable the accretion process to go on longer and then to reach final star masses well above the upper mass limit of spherically symmetric accretion. The two main theoretical scenarios both require the presence of a disk and high accretion rates: (a) a monolithic collapse scenario (Tan & McKee 2002; McKee & Tan 2003), also called turbulent core model; and (b) a highly dynamical competitive accretion model involving the formation of a cluster (Bonnell & Bate 2006). The turbulent core model implies supersonic turbulence in the protostellar envelope, while the competitive accretion model predicts cores that are subsonic, but still embedded in a supersonic envelope (see Krumholz & Bonnell 2009). Moreover, massive star formation triggered by converging turbulent flows is predicted by numerical simulations (e.g. Vázquez-Semadeni et al. 2007; Heitsch et al. 2008) and proposed for several objects (e.g. DR21(OH), Csengeri et al. 2011).

Several studies have been previously done on water chemistry in massive protostars, well before the golden age of IR satellites. Jacq et al. (1990) observed the $3_{13} - 2_{20}$ transition of $H_2^{18}O$ at 203 GHz, one of the very few thermal water lines observable from ground, toward several sources, including one presented in this paper, DR21(OH). They concluded that the water abundance is typically of order 10^{-5} (relative to H_2) or less in hot dense regions (where $T > 100$ K). While in cold regions water is mostly found as ice on dust grains, at temperatures $T > 100$ K the gas-phase water abundance increases by several orders of magnitudes as the ice evaporates (Fraser et al. 2001; Aikawa et al. 2008). A second increase occurs at $T \geq 250$ K, when gas-phase reactions drive all available oxygen into water (e.g., Charnley 1997; van Dishoeck et al. 2013). The launch of ISO and SWAS satellites offered the possibility to observe for the first time ro-vibrational fundamental bands of water in absorption against bright infrared continuum sources. Hence, the inner water abundance has been probed toward AFGL2591 by Helmich et al. (1996) and estimated to $2\text{--}6 \times 10^{-5}$, comparable to that of solid H_2O (van Dishoeck & Helmich 1996). Some uncertainties remain on the water content due to the low spectral resolution of the ISO data. The outer abundance (in re-

gion where $T < 100$ K) has been estimated to $0.8\text{--}13 \times 10^{-9}$ by Snell et al. (2000) using SWAS satellite data (from observation of the 557 GHz water line) in several sources (e.g. AFGL2591). Later Boonman et al. (2003) combined ISO-SWS/LWS/SWAS data to derive an abundance profile in a set of massive protostars, including W3IRS5 and AFGL2591. Their preferred scenario is a model with ice evaporation occurring at $T \sim 90 - 110$ K in the inner part ($\chi_{in} \sim 10^{-4}$) with a low outer water abundance ($\chi_{out} \sim 10^{-8}$). This jump-like radial profile for water has been confirmed by van der Tak et al. (2006) using new interferometric observations from the ground of the 203 GHz $H_2^{18}O$ line, and by the results of time-dependent gas-grain chemical modeling by Kaźmierczak-Barthel et al. (2015). Observing the same $H_2^{18}O$ line in younger sources including two of our sample, Marseille et al. (2010b) have not been able to constrain the inner abundance, but have derived a global water abundance of 5×10^{-8} and 5×10^{-7} , respectively for the HMPOs W43-MM1 and DR21(OH).

As shown by Chavarría et al. (2010), Herpin et al. (2012), or van der Wiel et al. (2013), from single-dish observations it is only possible to trace the dynamics of gas in the deeply embedded phase of star formation using spectrally resolved emission-line profiles. This has been done before with species like CS by van der Tak et al. (2000) and Shirley et al. (2003). Infall motion and supersonic turbulence in massive dense clouds have been further studied via HCN and CS surveys by Wu et al. (2010), or using HCO^+ and N_2H^+ by Schlingman et al. (2011). In addition, spectroscopic observations of the molecular content of the gas surrounding the protostellar object shed light on the complex chemistry occurring in these environments (e.g., Herpin et al. 2009; Benz et al. 2010; Bruderer et al. 2010; Wyrowski et al. 2010). Within the CHESS Herschel program (Ceccarelli et al. 2010), HIFI spectral survey of AFGL2591 has been performed, and the chemical structure of its protostellar envelope has been modeled by Kaźmierczak-Barthel et al. (2015). More generally, understanding the chemical evolution of HM protostars is now a very active field: for instance Gerner et al. (2014) have shown that the chemical composition evolves along with the evolutionary stages.

Probing star formation using spectroscopic observations of water was the major goal of the guaranteed-time key program *Water In Star-forming regions with Herschel* (WISH, van Dishoeck et al. 2011). Water was indeed one of the main drivers of the Herschel Space Observatory mission (hereafter Herschel, Pilbratt et al. 2010) and particularly of the HIFI spectroscopy instrument (de Graauw et al. 2010). The WISH program aims at characterizing the dynamics of the different components of the gas surrounding the central massive core and intends to measure the amount of cooling that water lines provide.

Table 2. Herschel/HIFI observed water line transitions in the source sample.

Species/transitions	Frequency ^b [GHz]	Wavelength [μ m]	E_u [K]	n_{crit}^c [cm ⁻³]	HIFI band	Beam [$''$]	η_{mb}	T_{sys} [K]	rms ^d [mK]
o-H ₂ ¹⁸ O 1 ₁₀ -1 ₀₁ ^a	547.6764	547.4	60.5	3.5×10^7	1a	37.8	0.62	80	27
o-H ₂ ¹⁷ O 1 ₁₀ -1 ₀₁	552.0209	543.1	61.0	3.5×10^7	1a	37.8	0.62	70	28
p-H ₂ ¹⁸ O 2 ₀₂ -1 ₁₁	994.6751	301.4	100.6	5.8×10^7	4a	21.1	0.63	290	44
o-H ₂ ¹⁸ O 3 ₁₂ -3 ₀₃	1095.6274	273.8	248.7	1.6×10^8	4b	19.9	0.63	380	32
p-H ₂ ¹⁸ O 1 ₁₁ -0 ₀₀	1101.6982	272.1	52.9	1.9×10^8	4b	19.9	0.63	390	20
p-H ₂ ¹⁷ O 1 ₁₁ -0 ₀₀	1107.1669	272.1	52.9	1.9×10^8	4b	19.9	0.63	380	32
o-H ₂ ¹⁷ O 2 ₁₂ -1 ₀₁	1662.4644	180.3	113.6	5.6×10^8	6b	12.7	0.58	1410	215
o-H ₂ O 1 ₁₀ -1 ₀₁ ^a	556.9361	538.3	61.0	3.5×10^7	1a	37.1	0.62	80	27
p-H ₂ O 2 ₁₁ -2 ₀₂	752.0332	398.6	136.9	7.1×10^7	2b	28.0	0.64	90	36
p-H ₂ O 5 ₂₄ -4 ₃₁	970.3150	309.0	598.8	9.0×10^6	4a	21.8	0.63	620	25
p-H ₂ O 2 ₀₂ -1 ₁₁	987.9268	303.5	100.8	5.8×10^7	4a	21.3	0.63	340	79
o-H ₂ O 3 ₁₂ -3 ₀₃	1097.3651	273.2	249.4	1.6×10^8	4b	19.9	0.63	380	32
p-H ₂ O 1 ₁₁ -0 ₀₀	1113.3430	269.0	53.4	1.9×10^8	4b	19.7	0.63	395	20
o-H ₂ O 2 ₂₁ -2 ₁₂	1661.0076	180.5	194.1	3.1×10^8	6b	12.7	0.58	1410	215
o-H ₂ O 2 ₁₂ -1 ₀₁	1669.9048	179.5	114.4	5.6×10^8	6b	12.6	0.58	1410	215

Notes. ^a This line was mapped in OTF mode. ^b Frequencies are from Pearson et al. (1991). ^c At 100 K. ^d The rms is the noise in $\delta\nu = 1.1$ MHz.

A sample of 19 massive protostars, covering all phases of high-mass star formation has been observed within WISH. In addition, 4 pre-stellar cores have been studied by Shipman et al. (2014). The velocity profiles of the low-excitation H₂O lines toward this sample have been presented by van der Tak et al. (2013), without detailed modeling. They decomposed HIFI water line spectra into three distinct physical components: (i) dense cores (protostellar envelopes) usually seen as medium or narrow absorption/emission; (ii) outflows seen as broader features; and (iii) absorptions by foreground clouds along the line of sight. More generally, the line profiles obtained in low- (Kristensen et al. 2010), intermediate- (Johnstone et al. 2010), and high-mass (see W3IRS5, Chavarría et al. 2010) young stellar objects exhibit similar velocity components (San José-García et al. 2013; Mottram et al. 2014): a broad (full width at half maximum FWHM ~ 25 km s⁻¹), a medium (~ 5 –10 km s⁻¹) one, and a narrower component (<5 km s⁻¹).

In this paper, we focus on the analysis of the water observations toward the mid-IR quiet massive protostars of the WISH sample. A similar study has been done by Choi *et al.* (in preparation) for mid-IR bright sources. Using the high velocity resolution of the HIFI instrument we study the dynamics of the gas, estimate the infall and turbulent velocities present in the protostellar envelopes, and derive the H₂O abundances in these sources. Sections 2 and 3 present our observations and source sample respectively. Results coming from Gaussian (water and other species) line fittings are given in Sect. 4, while detailed line analysis is given in Sect. 5. We then model the observations using a radiative transfer code in Sect. 6. We estimate the outflow and infall velocities, turbulent velocity, molecular abundances, and the physical structure of the sources. We finally discuss (Sect. 7) the results in terms of massive-star formation scenarios and compare them to previous studies, in particular Herpin et al. (2012).

2. Observations

Fourteen water lines (see Table 2) have been observed with HIFI at frequencies between 547 and 1670 GHz toward the whole source sample in 2010 and 2011 (list of observation identification numbers, *obsids*, are given in Appendix A.1). An additional

high-energy water line at 970.3150 GHz has been observed toward DR21(OH). The observations are part of the WISH GT-KP.

Data were taken simultaneously in H and V polarizations using both the acousto-optical Wide-Band Spectrometer (WBS) with 1.1 MHz resolution and the digital auto-correlator or High-Resolution Spectrometer (HRS) providing higher spectral resolution (125 kHz). We used the Double Beam Switch observing mode with a throw of 3'. The off positions have been inspected and do not show any H₂O or significant continuum emission. The frequencies, energy of the upper levels, system temperatures, integration times and rms noise level at a given spectral resolution for each of the lines are provided in Table 2. Calibration of the raw data into the T_A scale was performed by the in-orbit system (Roelfsema et al. 2012); conversion to T_{mb} was done using the latest beam efficiency estimate from October 2014¹ given in Table 2 and a forward efficiency of 0.96. HIFI receivers are double sideband with a sideband ratio close to unity (Roelfsema et al. 2012). The flux scale accuracy is estimated to be around 10% for bands 1 and 2, 15% for bands 3 and 4, and 20 % in bands 6 and 7¹. The frequency calibration accuracy is 20 kHz and 100 kHz (i.e. better than 0.06 km s⁻¹), respectively for HRS and WBS observations. Data calibration was performed in the Herschel Interactive Processing Environment (HIPE, Ott 2010) version 12.1. Further analysis like Gaussian fit was done within the CLASS² package. These lines are not expected to be polarized, thus, after inspection, data from the two polarizations were averaged together. For all observations, possible contamination from lines in the image sideband of the receiver has been checked and none was found. Because HIFI is operating in double-sideband, the measured continuum level has been divided by a factor of 2 (in the Figures and the Tables) to be directly compared to the single sideband line profiles (this is justified because the sideband gain ratio is close to 1).

3. The source sample

Five sources are studied here: NGC6334I(N), DR21(OH), IRAS16272-4837, and IRAS05358+3543 whose entire water

¹ <http://herschel.esac.esa.int/twiki/pub/Sandbox/TestHifiInfoPage/>

² <http://www.iram.fr/IRAMFR/GILDAS/>

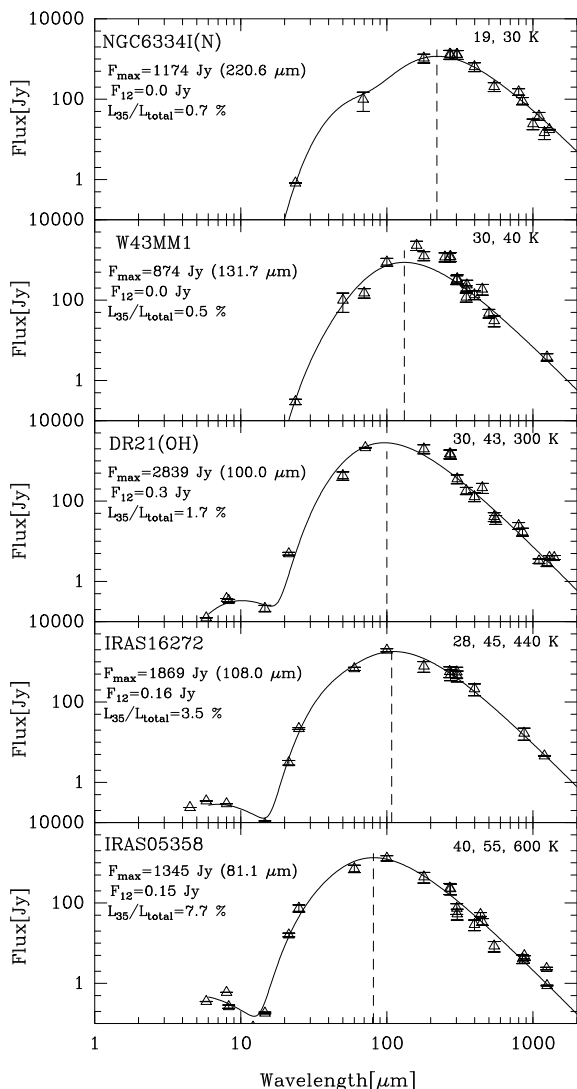


Fig. 1. Spectral energy distributions obtained from the 1D model overlaid on observed flux densities of each source. Peak flux densities in the millimeter range have been adjusted to fit the radial extent of the model. Each caption gives the temperatures of the black body components (top right), the maximum flux F_{\max} , and the corresponding wavelength of the SED, the flux F_{12} at $12\mu\text{m}$, and the contribution of the hot part (F_{35} , integrated flux for $\lambda < 35\mu\text{m}$) to the total integrated flux F_{total} (top left).

observations set is analyzed for the first time in this paper while W43-MM1 results have been presented in Herpin et al. (2012). The source coordinates, luminosity, distance, and velocities are given in Table 1. The position observed corresponds to the peak of the mm continuum emission from the literature (see van der Tak et al. 2013). The selected sources are mid IR-quiet dense cores (Motte et al. 2007), with bolometric luminosities $0.19\text{--}2.4 \cdot 10^4 L_{\odot}$ at distances $1.7\text{--}5.5$ kpc and sizes (radius) in mm continuum of $\sim 0.26\text{--}0.82$ pc (see Appendix C in van der Tak et al. 2013), hence larger than a $20''$ beam ($0.15\text{--}0.55$ pc at these distances). Even if these massive dense cores are expected to be fragmented on small scales, only a small fraction of the total mass is in individual fragments, except for the dominant central source (see references in the following for each source). As a consequence the large-scale, average-density profile of the cores applies well down to the smallest structures observable with HIFI.

The NGC6334 I(N) source, located in the northern part of the filament in the central region of NGC6334, has been extensively studied at mm/submm wavelengths (e.g. Hunter et al. 2006, 2014). Brogan et al. (2009) imaged NGC6334 I(N) at $\sim 2''$ angular resolution using the SMA. They detected a cluster of compact sources, SMA1-SMA7 (most of them within the HIFI beams), in the 1.3 mm dust continuum emission, with gas masses of $6\text{--}74 M_{\odot}$. Spectral line data show evidence of infall accelerating with depth into SMA1 and the presence of multiple outflows. Note that parameters for this source and NGC6334I were exchanged in van Dishoeck et al. (2011). Observation with HIFI of NGC6334I have been presented by Emprechtinger et al. (2013).

DR21(OH) is located in the Cygnus X region, in the dense DR 21 filamentary ridge, where active star formation and global infall motions are observed (Csengeri et al. 2011; Hennemann et al. 2012). Infall signatures in DR21(OH) are observed in low- J CS lines on the same spatial scale covered by our observations (Chandler et al. 1993). Girart et al. (2013) defined this rich molecular source as a highly fragmented, magnetized, turbulent dense core. The DR21(OH) core is formed by two main dusty condensations, MM 1 and MM 2, split into a cluster of dusty sources at scales of 1000 AU (Zapata et al. 2012). MM1 contains a hot core and shows centimeter continuum emission (Araya et al. 2009). Very active and powerful outflows are detected.

In contrast, less information is available about the more luminous ($L \sim 2.4 \cdot 10^4 L_{\odot}$) source IRAS16272-4837. From MSX observations and studies by Garay et al. (2007), this source can definitely be classified as a massive star-forming region in a very early evolutionary stage, a mid-IR quiet HMPO ($F_{21} = 2.2$ Jy). No radio continuum emission was detected. The 1.2 mm emission arises from a central component surrounded by more extended gas (region of $41'' \times 25''$, Faúndez et al. 2004) and the line profiles observed suggest that the molecular gas is undergoing infalling motions.

IRAS05358+3543 is a relatively low-luminosity ($L \sim 6.3 \cdot 10^3 L_{\odot}$) and nearby (1.8 kpc) massive dense core, composed of four main sources, all within a box of $4'' \times 6''$ (Leurini et al. 2007; Palau et al. 2014), hence within the Herschel telescope beam at all frequencies. Two of these sources are part of a protobinary system with a dynamical age of $\sim 3.6 \cdot 10^4$ yr (Beuther et al. 2007). Several molecular outflows are observed (Beuther et al. 2002a), but no infall is detected (Herpin et al. 2009). The integrated gas mass is estimated to $142 M_{\odot}$ by van der Tak et al. (2013). Leurini et al. (2007) suggest that the main source mm1a harbours a hot core with $T \sim 220$ ($75 < T < 330$) K and may contain a massive circumstellar disk. Because of its 21 microns flux density (11.9 Jy), this source is rather between the mid-IR quiet and mid-IR bright HMPO stages.

Continuum emission from our sources is determined with well-sampled observations from various telescopes including IRAS (archive³), Spitzer (archive⁴), MSX (archive⁵), JCMT (archive⁶), and Vallée & Fiege 2006; Sandell 2000; McCutcheon et al. 2000), KAO (Harvey et al. 1986; Lester et al. 1985), CSO (Motte et al. 2003), SMA (Beuther et al. 2007; Hunter et al. 2006), APEX, SEST (Garay et al. 2007; Muñoz et al. 2007), IRAM-30m (Beuther et al. 2002b; Motte et al. 2007), IRAM-PdB (Beuther et al. 2007), VLA (Beuther et al. 2002a; Rodríguez et al. 2007), ATCA

³ <http://irsa.ipac.caltech.edu/applications/IRAS/ISSA/>

⁴ <http://sha.ipac.caltech.edu/applications/Spitzer/SHA/>

⁵ <http://irsa.ipac.caltech.edu/Missions/msx.html>

⁶ <http://www.cadc-ccda.hia-ihp.nrc-cnrc.gc.ca/en/jcmt/>

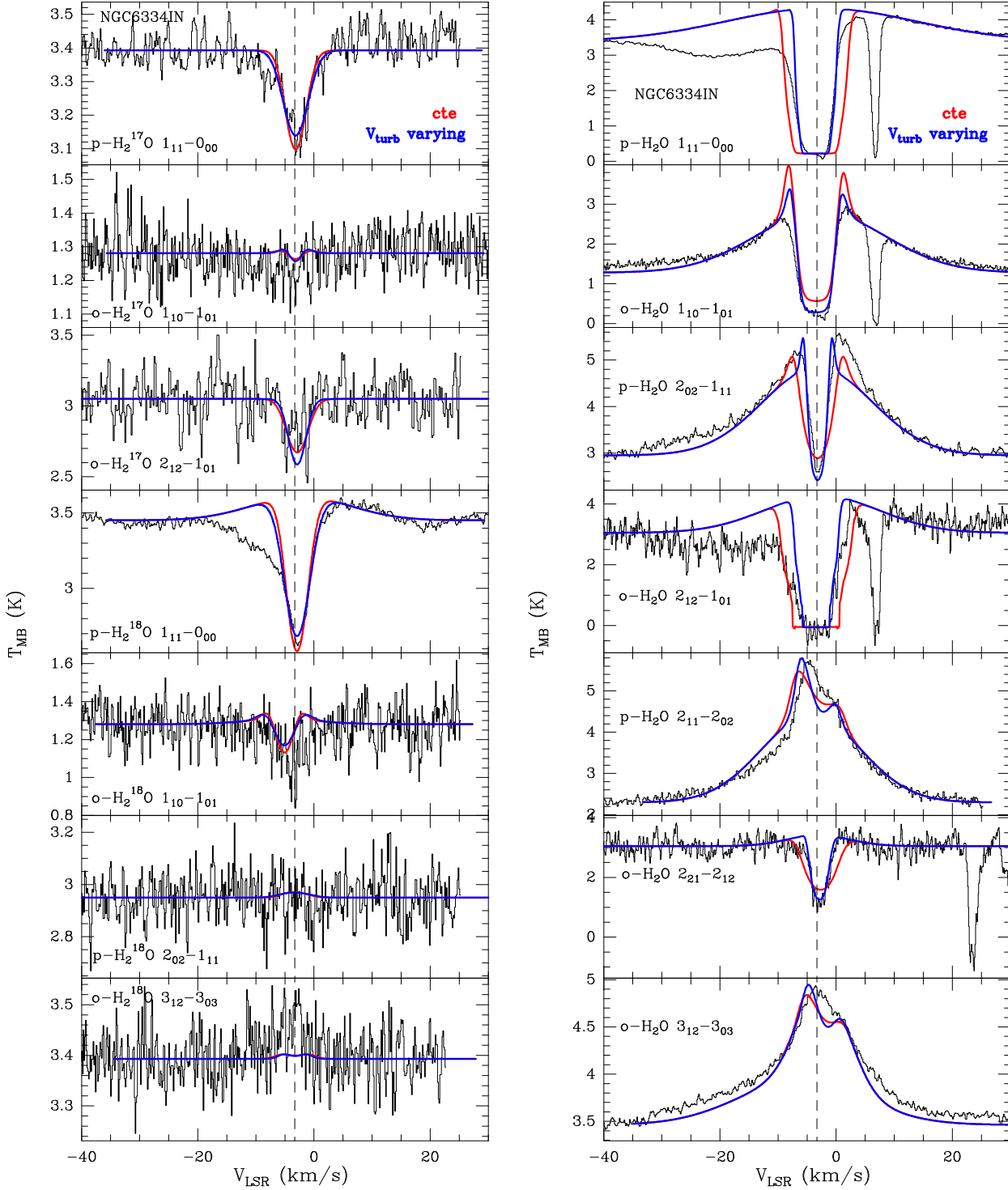


Fig. 2. HIFI spectra of H_2^{17}O and H_2^{18}O (Left) and H_2^{16}O (Right) lines (in black) with continuum for NGC6334I(N). The best-fit radiative transfer models are shown as red and blue lines over the spectra, respectively for constant parameters ($V_{\text{inf}} = -0.7$ and $V_{\text{turb}} = 2.5 \text{ km s}^{-1}$) and varying turbulent velocity. Vertical dotted lines indicate the V_{LSR} . The spectra have been smoothed to 0.2 km s^{-1} , and the continuum divided by a factor of two.

(Walsh et al. 1998; Beuther et al. 2008), OVRO (Woody et al. 1989), and Herschel-HIFI/PACS (van der Tak et al. 2013). In particular, flux densities below $35 \mu\text{m}$ come from Spitzer and MSX observations. Hence, the spectral energy distribution (SED) for these sources is particularly well constrained. Following the method of Herpin et al. (2009), we propose a rough evolutionary classification of our 5 objects from the fitted SEDs shown in Fig. 1 (the reference spatial resolution is the beam

of the observation at 1.1 or 1.2 mm, i.e. $11''$ with IRAM-30m for IRAS05358, W43MM1, and DR21(OH), and $24''$ with JCMT or SEST for the two other sources), using the following parameters:

- flux density at $12 \mu\text{m}$,
- flux density at $21 \mu\text{m}$,
- wavelength and flux density of the maximum continuum emission,

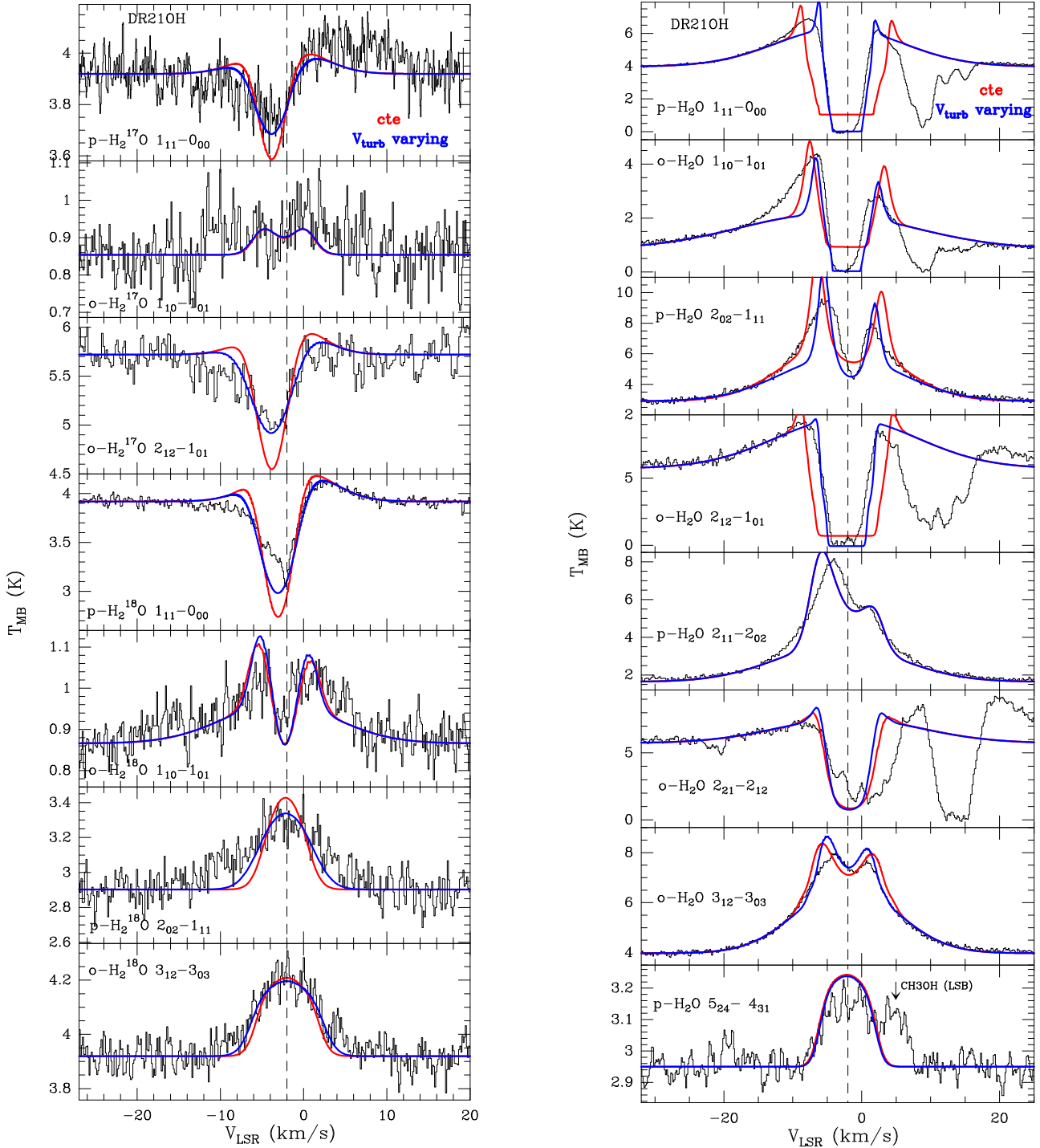


Fig. 3. As in Figure 2 but for DR21(OH) ($V_{inf} = -1.5$ and $V_{turb} = 2.5$ km s $^{-1}$ for the constant model). The p-H $_2$ O 5 $_{24}$ -4 $_{31}$ line is blended with the CH $_3$ OH line at 957.995737 GHz from the LSB.

- contribution of the hot part ($\lambda < 35$ μ m) to the total integrated flux.

In addition, we also use the evolutionary tracer $L^{0.6}M_{env}^{-1}$ first introduced by Bontemps et al. (1996) for low-mass objects: this quantity increases with the evolutionary status of the source. It is assumed that less evolved sources are colder, hence the SED peaks at longer wavelength with weaker flux. As the massive core evolves, it becomes warmer, thereby heating the dust. As a consequence, the contribution of the flux at shorter wavelength (F_{35} , the integrated flux density for $\lambda < 35$ μ m) increases.

Comparison of these quantities (Table 1) leads to the following evolutionary sequence going from youngest to older: NGC64334I(N) \rightarrow W43-MM1 \rightarrow DR21(OH) \rightarrow IRAS16272-4837 \rightarrow IRAS05358+3543. The fact that three different estimates give the same order lends credibility to this sequence. We adopt this sequence for the following discussion. Nevertheless, we note that the order of DR21(OH) and IRAS16272-4837 can be inverted if one uses the $L^{0.6}M_{env}^{-1}$ criterion only (see values in Table 1) or if we consider that DR21(OH) harbours a hot core as IRAS05358.

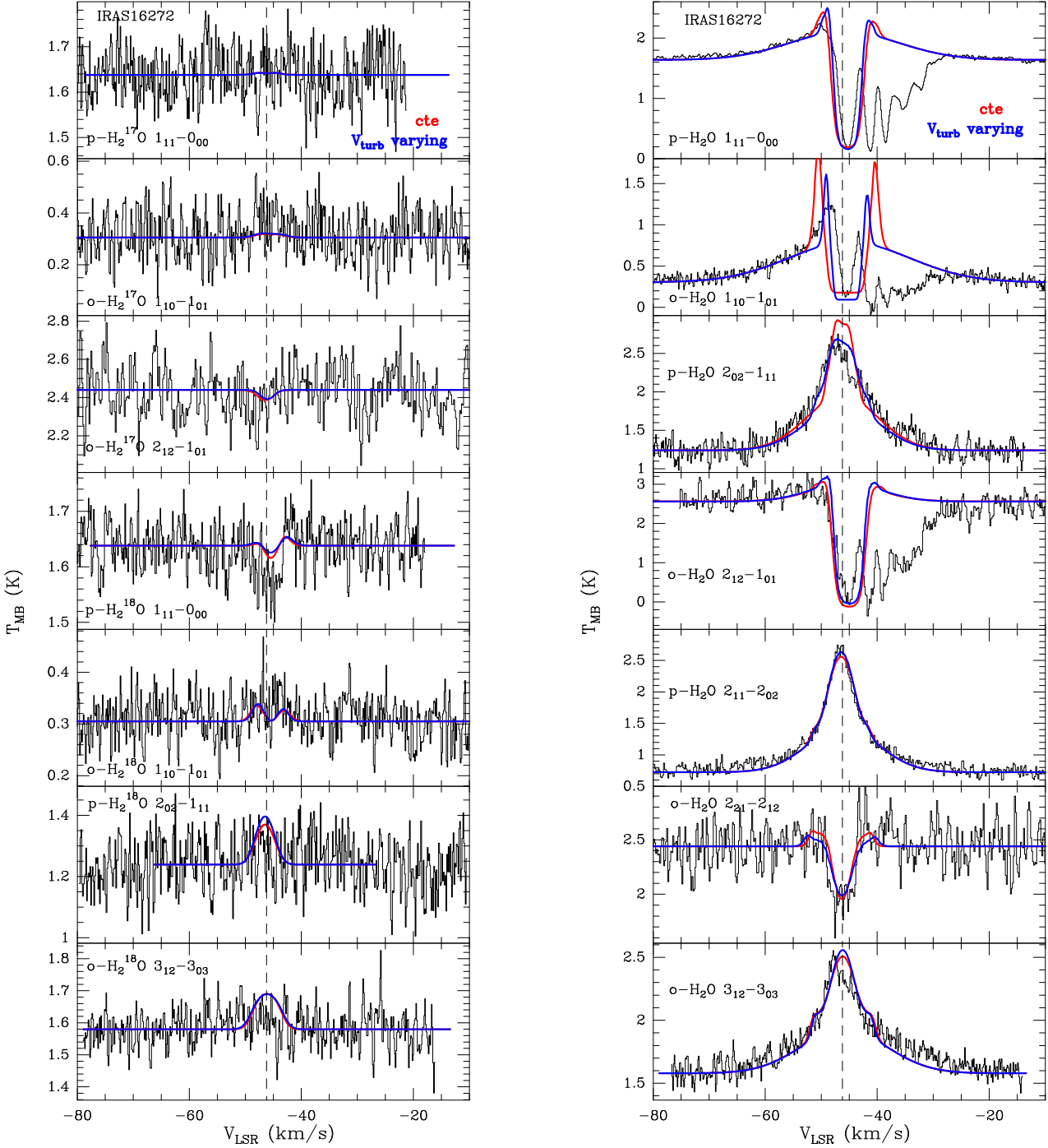


Fig. 4. As in Figure 2 but for IRAS16272 ($V_{inf} = -0.2$ and $V_{turb} = 2.2$ km s⁻¹ for the constant model).

4. Results

The spectra including continuum emission are presented in Fig. 2-5 for the rare isotopologues (H₂¹⁷O, H₂¹⁸O) and H₂¹⁶O for all sources, except W43-MM1 which was presented in Herpin et al. (2012). Spectra of the H₂O 1₁₁-0₀₀ (and H₂¹⁸O), 2₀₂-1₁₁, and 2₁₂-1₀₁ lines have also been included in van der Tak et al. (2013). In addition, Fig. B.1-B.3 in Appendix B display lines from other species than water that are serendipitously covered in our data. In most cases, we show the HRS spectra, except for the ground-state p-H₂¹⁸O 1₁₁-0₀₀, p-H₂O 1₁₁-0₀₀, and o-H₂O 2₁₂-1₀₁ lines, where WBS spectra were used since the velocity range covered by the HRS was insufficient to show the broad component. In a few cases (e.g. o-H₂O 2₁₂-1₀₁ spectra in NGC6334I(N)), the

detected absorption is slightly below the continuum but within the flux uncertainties (see Sect. 2).

Several foreground clouds (van der Tak et al. 2013) contribute to the spectra in NGC6334I(N), DR21(OH) and IRAS16272 in terms of water absorption at V_{LSR} shifted with respect to source velocity in the o-H₂O 1₁₀-1₀₁, p-H₂O 1₁₁-0₀₀ and o-H₂O 2₁₂-1₀₁ lines spectra (absorption is also visible in the o-H₂O 2₂₁-2₁₂ spectra in DR21(OH)). These foreground clouds are not analyzed here.

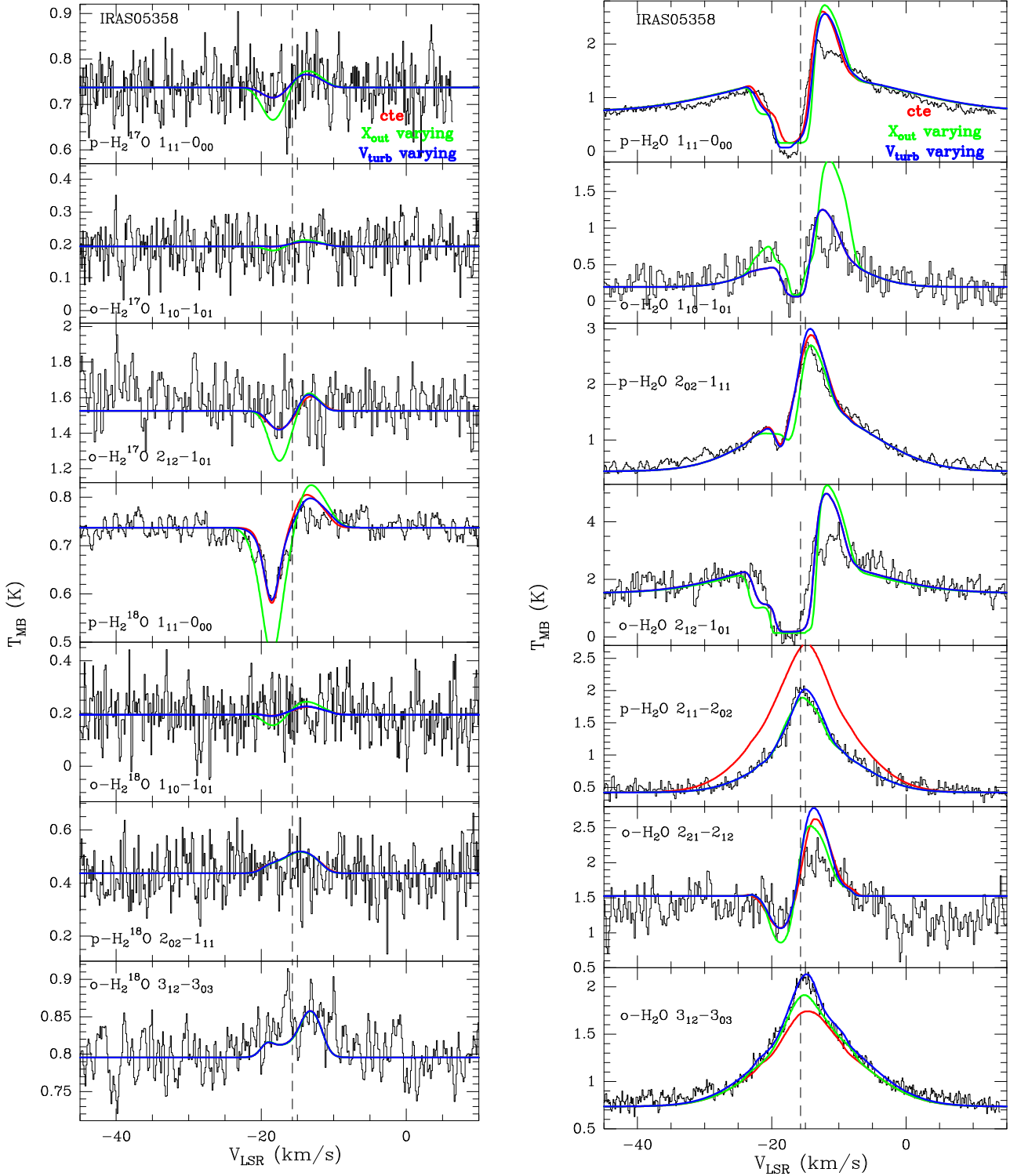


Fig. 5. As in Figure 2 but for IRAS05358 ($V_{inf} = +3.0$ and $V_{turb} = 2.0$ km s $^{-1}$ for the constant model), more (in green) a varying outer abundance model (see Sect. 6.3)

4.1. Velocity components

For each transition, we derive the peak, or minimum (in case of absorption), main-beam and continuum temperatures, the full-width at zero intensity (FWZI, see Mottram et al. 2014, for details), half power line-widths for the different line components from multi-component Gaussian fits, and opacities for lines in

absorption. Line parameters are given in Tables 3-6. An example of the Gaussian fits is given for IRAS05358 in Appendix C. Our results are consistent with van der Tak et al. (2013) and San Jose-Garcia et al. (2015) and do not depend on the adopted method.

We will follow the terminology adopted in previous WISH papers (e.g. Johnstone et al. 2010; Kristensen et al. 2010;

Table 3. Observed line emission parameters for the detected lines toward NGC6334I(N). V is the Gaussian component peak velocity. ΔV is the velocity full width at half-maximum (FWHM) of the narrow, medium and broad components. FWZI is the full-width at zero intensity. The opacity τ is from absorption lines.

Line	T_{mb} [K]	T_{cont} [K]	FWZI [km s ⁻¹]	V_{nar} [km s ⁻¹]	ΔV_{nar} [km s ⁻¹]	V_{med} [km s ⁻¹]	ΔV_{med} [km s ⁻¹]	V_{br} [km s ⁻¹]	ΔV_{br} [km s ⁻¹]	τ
o-H ₂ ¹⁸ O 1 ₁₀ -1 ₀₁	1.10	1.28	14.6			-3.8±0.4 ^a	6±1			0.15±0.03
o-H ₂ ¹⁸ O 3 ₁₂ -3 ₀₃	0.09	3.42	13.7			-3.9±0.4	6±1			
p-H ₂ ¹⁸ O 1 ₁₁ -0 ₀₀ ^b	2.63	3.45	45.6	-2.9 ±0.2 ^a	4.5±0.2					0.27±0.05
p-H ₂ ¹⁷ O 1 ₁₁ -0 ₀₀ ^b	3.10	3.42	24.2			-3.0±0.2 ^a	5.7±0.5			0.10±0.02
o-H ₂ ¹⁷ O 2 ₁₂ -1 ₀₁	2.56	3.05	5.0	-3.3±0.3 ^a	4.2±0.5					0.17±0.06
o-H ₂ O 1 ₁₀ -1 ₀₁	0.0	1.28	92.2			-3.5±0.1 ^a	5.8±0.2	-2.0±0.2	26.1±0.6	> 5
p-H ₂ O 2 ₁₁ -2 ₀₂	5.85	2.30	90.4			-3.2±0.1	7.3±0.3	-4.4±0.2	29.4±0.7	
p-H ₂ O 2 ₀₂ -1 ₁₁	2.31	2.95	58.1	-3.0±0.1 ^a	3.1±0.1	-3.0±0.2	10.0±0.3	-5.7±0.2	29.6±0.5	0.24±0.05
o-H ₂ O 3 ₁₂ -3 ₀₃	4.91	3.48	82.6			-1.9±0.1	9.6±0.3	-6.1±0.3	27.6±0.6	
p-H ₂ O 1 ₁₁ -0 ₀₀ ^b	0.06	3.48	98.0			-3.9±0.2 ^a	6.1±0.3	-3±2	30±1	4.1±0.6
o-H ₂ O 2 ₂₁ -2 ₁₂	1.20	3.05	6.0	-2.8±0.2 ^a	2.9±0.4					0.9±0.3
o-H ₂ O 2 ₁₂ -1 ₀₁ ^b	0.0	3.05	27.4			-3.9±0.2 ^a	6.8±0.4			> 5

Notes. ^a in absorption, ^b WBS data**Table 4.** Observed line emission parameters for the detected lines toward DR21(OH). V is the Gaussian component peak velocity. ΔV is the velocity full width at half-maximum (FWHM) of the narrow, medium and broad components. FWZI is the full-width at zero intensity. The opacity τ is from absorption lines.

Line	T_{mb} [K]	T_{cont} [K]	FWZI [km s ⁻¹]	V_{nar} [km s ⁻¹]	ΔV_{nar} [km s ⁻¹]	V_{med} [km s ⁻¹]	ΔV_{med} [km s ⁻¹]	V_{br} [km s ⁻¹]	ΔV_{br} [km s ⁻¹]	τ
o-H ₂ ¹⁸ O 1 ₁₀ -1 ₀₁	1.04	0.87	40.0	-2.7 ±0.2 ^a	1.4 ±0.3			-1.5±0.3	16.3±0.8	
o-H ₂ ¹⁷ O 1 ₁₀ -1 ₀₁	0.96	0.85	19.8					-1.6±0.8	15±2	
p-H ₂ ¹⁸ O 2 ₀₂ -1 ₁₁	3.36	2.90	24.4					-2.5±0.2	12.0±0.4	
o-H ₂ ¹⁸ O 3 ₁₂ -3 ₀₃	4.25	3.92	21.2			-1.9±0.1	8.6±0.3			
p-H ₂ ¹⁸ O 1 ₁₁ -0 ₀₀	3.04	3.92	35.4	-2.1±0.1 ^a	0.8±0.1	-2.5±0.2 ^a	5.7±0.2	0±0.6	10±0.6	0.25±0.05
p-H ₂ ¹⁷ O 1 ₁₁ -0 ₀₀	3.77	3.92	26.9			-3.6±0.2 ^a	5.3±0.7	0±1	12±2	0.04±0.01
o-H ₂ ¹⁷ O 2 ₁₂ -1 ₀₁	5.12	5.72	25.7	-4.2±0.2 ^a	4.4±0.4					0.11±0.04
o-H ₂ O 1 ₁₀ -1 ₀₁	0.0	0.85	85.7			-2.7±0.2 ^a	5.6±0.1	-1.9±0.2	22.4±0.3	> 5
p-H ₂ O 2 ₁₁ -2 ₀₂	8.19	1.65	62.7			-3.0±0.1	8.3±0.1	-3.1±0.1	22.3±0.3	
p-H ₂ O 5 ₂₄ -4 ₃₁ ^b	3.25	2.95	26.0			-1.4±0.3	9.9±0.6			
p-H ₂ O 2 ₀₂ -1 ₁₁	9.40	2.90	51.3	-1.7±0.1 ^a	3.7±0.1	-2.6±0.1	8.2±0.1	-2.9±0.1	20.4±0.2	
o-H ₂ O 3 ₁₂ -3 ₀₃	7.93	3.98	52.5	-1.7±0.1	2.9±0.2	-2.5±0.1	9.9 ±0.1	-1.9±0.1	20.4±0.3	
p-H ₂ O 1 ₁₁ -0 ₀₀	0.0	3.98	51.7	-3.5±0.2 ^a	4.6±0.2			-1.7±0.1	21.6±0.2	> 5
o-H ₂ O 2 ₂₁ -2 ₁₂ ^c	1.06	5.73	10.8			0.3±0.2 ^a	6.3±0.4			1.7±0.5
o-H ₂ O 2 ₁₂ -1 ₀₁ ^{b, c}	0.0	5.73	50.2	-2.4±0.2 ^a	4.1±0.2			-1.9±0.1	24.1±0.5	> 5

Notes. ^a in absorption, ^b WBS data, ^c blended with o-H₂O 2₁₂-1₀₁

Herpin et al. 2012): narrow (<5 km s⁻¹), medium (FWHM≈5-10 km s⁻¹), and broad (FWHM≈20-35 km s⁻¹). The narrow component centered at the source velocity is characterized by small FWHM and offset velocity, and is called *envelope component*, i.e. emission from the quiescent envelope, the signature of the passively heated envelope. Both broad and medium components arise in *cavity shocks*, i.e. shocks along the cavity walls according to the model of Mottram et al. (2014). The medium component is a narrower version of the broad component (also called *narrow outflow* by van der Tak et al. 2013), coming from a thin layer (1-30 AU) along the outflow cavity where non-dissociative shocks occur. A different physical component, called the medium offset component, with a velocity offset of at least a few km/s, is observed in low-mass objects and

is associated with spot shocks, i.e., dissociative shocks in the jet itself or at the base of the outflow (Mottram et al. 2014). This component is seen in the HM data by van der Tak et al. (2013) as a narrow outflow in absorption in the 1113 and 1669 GHz water lines and slightly offset from the envelope velocity.

4.2. Water Lines

4.2.1. Rare isotopologues

The more evolved objects, IRAS05358 and IRAS16272, exhibit fewer and weaker rare isotopologue lines, with no H₂¹⁷O detection. This is not due to a lower source luminosity or a larger distance as can be inferred from Table 1: e.g. IRAS16272-4837 ex-

Table 5. Observed line emission parameters for the detected lines toward IRAS16272. V is the Gaussian component peak velocity. ΔV is the velocity full width at half-maximum (FWHM) of the narrow, medium and broad components. FWZI is the full-width at zero intensity. The opacity τ is from absorption lines. Values within brackets stand for tentative detection.

Line	T_{mb} [K]	T_{cont} [K]	FWZI [km s ⁻¹]	V_{nar} [km s ⁻¹]	ΔV_{nar} [km s ⁻¹]	V_{med} [km s ⁻¹]	ΔV_{med} [km s ⁻¹]	V_{br} [km s ⁻¹]	ΔV_{br} [km s ⁻¹]	τ
o-H ₂ ¹⁸ O 1 ₁₀ -1 ₀₁	(0.34)	(0.30)	(8.1)			-45.1±0.7	6±1			
p-H ₂ ¹⁸ O 1 ₁₁ -0 ₀₀	1.54	1.64	5.7	-46.0±0.3 ^a	3.8±0.4					0.06±0.01
o-H ₂ O 1 ₁₀ -1 ₀₁	0.12	0.30	80.2	-45.8±0.1 ^a	2.1±0.1	-47±1	7±1	-45.0±0.6	28±2	0.9±0.1
p-H ₂ O 2 ₁₁ -2 ₀₂	2.80	0.73	59.9			-46.6±0.1	5.0±0.1	-46.3±0.1	20.1±0.1	
p-H ₂ O 2 ₀₂ -1 ₁₁	2.67	1.24	36.0	-47.7±0.2	2.8±0.4			-47.3±0.2	20.9±0.1	
o-H ₂ O 3 ₁₂ -3 ₀₃	2.50	1.58	46.0			-46.7±0.1	5.0±0.3	-45.0±0.3	23.7±0.7	
p-H ₂ O 1 ₁₁ -0 ₀₀ ^b	0.20	1.64	63.7	-45.3±0.2 ^a	3.0±0.2			-45.3±0.2	24.0±0.3	2.1±0.3
o-H ₂ O 2 ₂₁ -2 ₁₂	1.90	2.44	15.9	-46.5±0.2 ^a	3.5±0.2					0.25±0.05
o-H ₂ O 2 ₁₂ -1 ₀₁ ^b	0.0	2.44	50.0	-45.7±0.1 ^a	3.1±0.1			(-47±2)	(30±5)	> 5

Notes. ^a in absorption, ^b WBS data

Table 6. Observed line emission parameters for the detected water lines toward IRAS05358. V is the Gaussian component peak velocity. ΔV is the velocity full width at half-maximum (FWHM) of the narrow, medium and broad components. FWZI is the full-width at zero intensity. The opacity τ is from absorption lines.

Line	T_{mb} [K]	T_{cont} [K]	FWZI [km s ⁻¹]	V_{nar} [km s ⁻¹]	ΔV_{nar} [km s ⁻¹]	V_{med} [km s ⁻¹]	ΔV_{med} [km s ⁻¹]	V_{br} [km s ⁻¹]	ΔV_{br} [km s ⁻¹]	τ
p-H ₂ ¹⁸ O 1 ₁₁ -0 ₀₀	0.58	0.74	21.8	-18.1±0.1 ^a	2.5±0.3					0.24±0.06
o-H ₂ ¹⁸ O 3 ₁₂ -3 ₀₃	0.87	0.80	14.1			-14.1±0.4	9.0±0.8			
o-H ₂ O 1 ₁₀ -1 ₀₁	0.0	0.20	26.4	-16.9±0.3 ^a	3.0±0.2			-14.9±0.3	13.9±0.7	> 5
p-H ₂ O 2 ₁₁ -2 ₀₂	2.17	0.42	52.1	-15.3±0.1	4.5±0.2			-13.8±0.2	17.0±0.4	
p-H ₂ O 2 ₀₂ -1 ₁₁	2.72	0.44	55.6	-18.7±0.1 ^a	1.7±0.2	-13.9±0.1	5.0±0.2	-12.9±0.4	23.6±0.5	
o-H ₂ O 3 ₁₂ -3 ₀₃	2.18	0.74	56.2			-15.1±0.1	6.2±0.3	-13.7±0.2	21.0±0.2	
p-H ₂ O 1 ₁₁ -0 ₀₀	0.0	0.74	50.7	-16.5±0.3 ^a	4.9±0.3	-14.6±0.3	5.9±0.3	-13.3±0.3	20.6±0.3	> 5
o-H ₂ O 2 ₂₁ -2 ₁₂	1.0	1.52	25.5	-18.1±0.3 ^a	3.1±0.5			-12.6±0.4	10.9±0.8	0.4±0.1
o-H ₂ O 2 ₁₂ -1 ₀₁	0.0	1.52	26.3			-17.7±0.2 ^a	5.6±0.3	-13.8±0.4	20.3±0.8	> 5

Notes. ^a in absorption.

hibits a luminosity similar to that of W43-MM1 and is closer to us. The para ground state line p-H₂¹⁸O 1₁₁-0₀₀ is detected, as well as the o-H₂¹⁸O 3₁₂-3₀₃ in IRAS05358, but the o-H₂¹⁸O 1₁₀-1₀₁ line is not detected in IRAS16272 and IRAS05358. The fact that no H₂¹⁷O and no o-H₂¹⁸O 1₁₀-1₀₁ line are detected in IRAS16272 and IRAS05358 is likely due to lower water column densities, hence insufficient S/N ratio.

On the other hand, H₂¹⁷O lines are detected in the two other objects. The strongest H₂¹⁷O and H₂¹⁸O lines are found in DR21(OH). In this source, all observed rare isotopologue lines are detected.

The p-H₂¹⁸O 1₁₁-0₀₀, o-H₂¹⁷O 2₁₂-1₀₁, and p-H₂¹⁷O 1₁₁-0₀₀ lines appear in absorption, and broad signatures from the cavity shocks (red component in emission while the blue one is absorbed) are observed for DR21(OH) and NGC6334I(N). The o-H₂¹⁸O 1₁₀-1₀₁ line is in absorption for NGC6334I(N) while it is a blend of absorption (at line center) and emission in DR21(OH). The two other detected H₂¹⁸O lines, 2₀₂-1₁₁ and 3₁₂-3₀₃, arising from more excited energy levels, are in emission.

Most of the H₂¹⁷O/H₂¹⁸O line profiles for all sources but W43-MM1 exhibit an envelope component in absorption. We interpret this absorption as resulting from cold material in front of the

passively heated envelope. A medium component is detected in several lines too.

4.2.2. H₂¹⁶O

All H₂¹⁶O lines listed in Table 2 are detected toward all 4 sources and the global shape of the line profile for each line is similar from source to source (including W43-MM1): ground state lines are deeply absorbed and all lines (except p-H₂O 5₂₄-4₃₁) exhibit a broad component (blue component in absorption for NGC6334I(N)). In addition, line profiles consist of a narrow or medium component depending on the source and the line. The p-H₂O 2₀₂-1₁₁ and p-H₂O 2₁₁-2₀₂ lines are asymmetric (see section 5.3) due to the infall or expansion of the gas. The o-H₂O 2₂₁-2₁₂ line is in absorption except for IRAS05358 for which some emission is present too. The o-H₂O 3₁₂-3₀₃ line is dominated by the broad and medium components in emission.

For the only source, DR21(OH), where the p-H₂O 5₂₄-4₃₁ line has been observed, a medium component, slightly redshifted (by 1.7 km s⁻¹), is observed in emission, but blended with a methanol line from the lower sideband at 957.995737 GHz.

Broad, medium, and narrow velocity components are detected in all sources. We observe for the envelope component

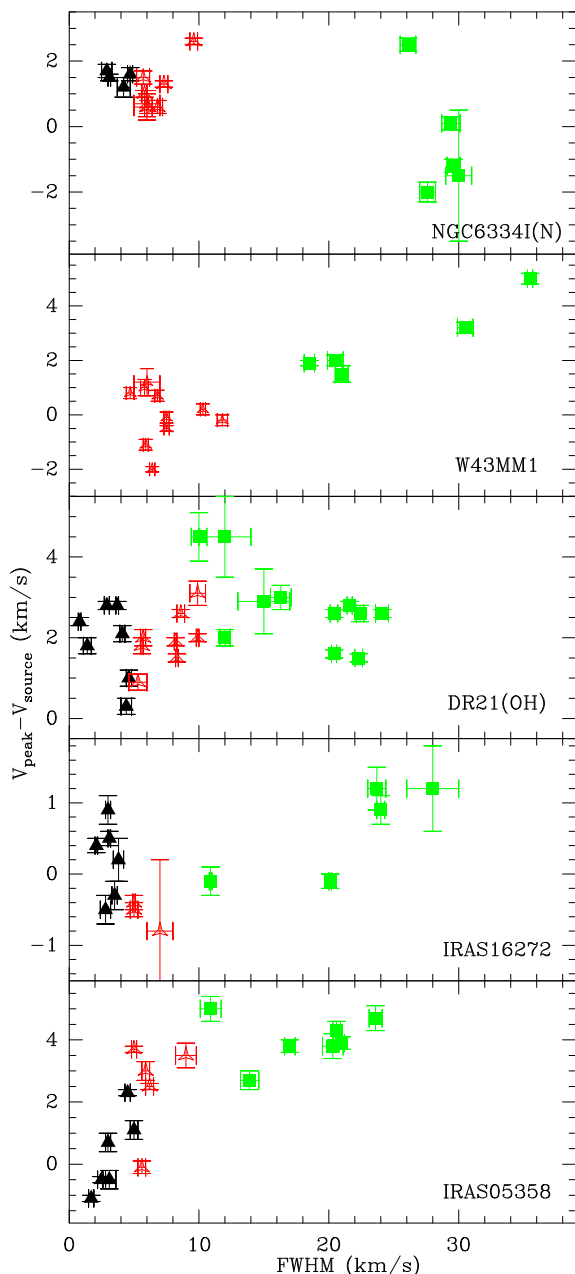


Fig. 6. FWHM versus offset of the peak from the source velocity for the gaussian velocity components found in the water (H_2^{16}O and H_2^{18}O) line profiles. Filled stars (black), empty stars (red), and filled squares (green) represent respectively the narrow, medium, and broad components.

a similar mean FWHM value of 3 km s^{-1} for IRAS16272 (± 0.5) and NGC6334I(N) (± 0.1), $3.5 (\pm 1.3) \text{ km s}^{-1}$ for IRAS05358, and $3.8 (\pm 0.7) \text{ km s}^{-1}$ for DR21(OH). The width of the medium component is clearly larger for the less evolved sources (7.1 ± 1.5 , 8 ± 2 , and $8.0 \pm 1.8 \text{ km s}^{-1}$ respectively for NGC6334I(N), W43-MM1, and DR21(OH)) than for IRAS16272 ($5.7 \pm 1.3 \text{ km s}^{-1}$) and IRAS05358 ($5.7 \pm 0.5 \text{ km s}^{-1}$). The FWHM of the broad component decreases from more than 25 km s^{-1} for NGC6334I(N) and W43-MM1 to roughly 20 km s^{-1} for the three other objects. Figure 6 shows that no or small velocity offset is observed for different components: only IRAS05358 and W43-MM1 exhibit offset increasing with FWHM (see section 5.1 for a trend analysis).

4.3. Other species

Several other species have been detected toward all sources within the 4 GHz wide WBS spectra (see Tables B.1-B.5): CH_3OH , ^{13}CO ($J=5-4$ and $10-9$), C^{18}O ($J=9-8$), CS ($11-10$), and H_2S ($3_{0,3} - 2_{1,2}$). These lines are detected in all sources in emission.

In addition to the bulk of methanol lines with $E_u \leq 200 \text{ K}$ observed in the entire sample, lines involving upper energy level up to 291, 434, and 514 K are detected respectively in NGC6334I(N), W43-MM1/IRAS16272, and DR21(OH). These lines exhibit an envelope and/or a medium component (and for one or two lines a broad component) similar to what is observed for water lines.

Both detected ^{13}CO $J=5-4$ and $10-9$ lines exhibit similar profiles, even if the $5-4$ line in DR21(OH) is much more self-absorbed at the center because of higher opacity. In addition to the C^{18}O $J=9-8$ line, the C^{18}O $J=10-9$ transition has been detected toward all sources but IRAS16272. For each species we note that the line widths are similar for both observed transition, and the velocity components derived from the Gaussian fitting are consistent with San José-García et al. (2013) (even if our narrow and medium components are only one single component for them in a few cases as they only distinguish between FWHM smaller or larger than 7.5 km s^{-1}).

The water cation H_2O^+ ($1_{11} - 0_{00}$, $J = 3/2 - 1/2$) is detected, in absorption, in all sources, except NGC6334I(N): its velocity components indicate that it likely originates from the envelope or outflow for IRAS05358 and W43-MM1 (see also Benz et al. 2010; Wyrowski et al. 2010, for other high-mass sources), while for DR21(OH) and IRAS16272 the absorption is redshifted by $5-10 \text{ km s}^{-1}$ and then very likely associated to the foreground clouds described before. In addition, the H_3O^+ cation is detected in absorption in W43-MM1, but is weaker than the H_2O^+ line, which, as stressed by Wyrowski et al. (2010), is unexpected.

More species are detected toward the 3 less evolved sources: deuterated water (HDO) and methyl formate (CH_3OCHO) for instance (see Appendix B). But more generally, DR21(OH) is the richest source with twice as many lines detected: the rare isotopologue ^{13}CS , many more methanol lines, dimethyl ether (CH_3OCH_3), CH^+ and OH^+ in absorption, H_2CO , ^{34}SO , OS^{18}O , and many lines of SO_2 .

All these lines peak at a mean velocity of $V_{\text{LSR}} = -15.9 \pm 0.3$, 46.5 ± 1.9 , -3.3 ± 0.8 , -4.0 ± 0.6 , and $98.4 \pm 1.2 \text{ km s}^{-1}$ respectively for IRAS05358, IRAS16272, DR21(OH), NGC6334I(N), and W43-MM1, hence similar to the source velocity, except for IRAS05358 whose lines are slightly red-shifted.

5. Analysis

5.1. Kinematics

For each source, we have searched for a correlation between FWHM and the velocity of the peak of various water components (see Fig.6). Such a correlation (both increasing together) has been found by Mottram et al. (2014) for Class 0 and I low-mass protostars. A general correlation is observed for IRAS05358 and W43-MM1: the velocity offset of each component increases with FWHM, hence the broad component is more and more red-shifted as the FWHM increases. This could mean that for outflows we see stronger red lobes (T_{ex} higher in the inner part) than blue lobes (where we see the outer part with lower T_{ex}). This trend is seen within the set of envelope and broad components for IRAS05358 but only clearly for the broad component in W43-MM1. For IRAS16272, a correlation is observed

Table 7. H_2^{16}O integrated line intensity ratios (not corrected for different beam sizes) for all sources for the broad velocity component. If available the ratio for the medium velocity component is given and noted (m). Optically thin and thick ratios are calculated for $T_{\text{ex}} = 100$ and 300 K.

Transitions	Observed ratio					LTE (100/300)		θ_1/θ_2^a
	NGC6334I(N)	W43MM1	DR21(OH)	IRAS16272	IRAS05358	Thin	Thick	
$1_{10} - 1_{01}/2_{12} - 1_{01}$			0.56 ± 0.06		0.20 ± 0.08	0.6/0.4	1.3/1.1	3.0
$1_{11} - 0_{00}/2_{02} - 1_{11}$			1.03 ± 0.05	0.9 ± 0.1	0.56 ± 0.06	2.4/1.7	1.3/1.1	0.9
(m)					1.2 ± 0.3			
$2_{11} - 2_{02}/2_{02} - 1_{11}$	1.14 ± 0.05	1.04 ± 0.06	0.88 ± 0.05	0.94 ± 0.05	0.60 ± 0.05	1.4/1.8	1.2/1.1	1.3
(m)			0.38 ± 0.05	3.0 ± 0.1	0.70 ± 0.06			

Notes. ^a Beam size ratio

for the broad component while nothing is seen for DR21(OH). NGC6334I(N) tends to show a decrease of $V_{\text{peak}} - V_{\text{source}}$ with FWHM. Surprisingly, the broad component tends to be blue-shifted with respect to the two other velocity categories. Whatever the source, no clear trend is seen for the medium component.

Hence, for W43-MM1 and IRAS05358 the different components globally lie in different regions of the FWHM vs. offset parameter space. We can then conclude that these components are formed under different conditions. Obviously, the same conclusion applies to the broad and narrow/medium components for NGC6334I(N) and perhaps for IRAS16272, but on the contrary no significant trend is observed for DR21(OH).

5.2. Outflow

We have used RADEX (van der Tak et al. 2007) to roughly estimate the column density of the H_2O in the outflow component for each source, assuming an isothermal homogenous material, shielding envelope emission. Following van der Tak et al. (2010) and Herpin et al. (2012), we adopt $n(\text{H}_2) = 3 \times 10^4 \text{ cm}^{-3}$ and $T_{\text{kin}} = 200 \text{ K}$, but also test neighboring values. The water column density necessary to retrieve the observed intensities and reproduce the observed line ratios for the broad component as derived from the Gaussian fitting (see Sect. 4.1 and Tables 3-6) is 10^{17} , 1.2×10^{17} , 4×10^{16} , and $8 \times 10^{16} \text{ cm}^{-2}$, respectively for NGC6334I(N), DR21(OH) (with $T_{\text{kin}} = 300 \text{ K}$ for this source), IRAS16272, and IRAS05358. These values are not sensitive to variations by less than 25% of T_{kin} . In Sect. 7.2 the formation of water in the outflow is studied.

5.3. Line asymmetries

Compared to optically thin lines (e.g. C^{18}O 9-8 and ^{13}CO 10-9 in most cases), most of the water-line profiles observed in our sources show clear asymmetries, revealing gas motions. Indeed, outflows, infall, and rotation can produce very specific line profiles with characteristic signatures (see Fuller et al. 2005, and references therein).

For all sources but IRAS05358, blue asymmetric (optically thick) lines, i.e. inverse P-Cygni profiles, are observed, hence likely indicating infalling material. In some circumstances, outflow or rotation could also produce a blue asymmetric line profile along a particular line of sight to the source. In IRAS05358 all lines but p- H_2O $2_{11}-2_{02}$ and o- H_2O $3_{12}-3_{03}$ have stronger red-shifted emission than blue-shifted emission (see Sec. 5.1) with a strong self-absorption dip at the source velocity, i.e. a P-Cygni profile, typical of expansion.

For IRAS16272, only the p- H_2O $2_{02}-1_{11}$ line exhibits this asymmetry, the other lines being either not optically thick enough, or contaminated by foreground clouds (for ground-state lines). Toward DR21(OH), a marked inverse P-Cygni profile is observed for the p- H_2O $2_{11}-2_{02}$ and p- H_2O $2_{02}-1_{11}$ lines, and weakly for o- H_2O $3_{12}-3_{03}$, whose almost symmetric double-horn profile might be produced by the outflow (Fuller et al. 2005). The p- H_2O $2_{11}-2_{02}$ and o- H_2O $3_{12}-3_{03}$ line profiles, which have a slightly stronger blue peak than the red one, exhibit a strong self-absorption dip at the source velocity. The H_2^{17}O and H_2^{18}O absorption lines do not show clear asymmetry, but are blue-shifted relative to the source velocity, as expected in the case of infall.

The case of NGC6334I(N) is less clear cut as the absorption of the blue component of the outflow in several lines complicates the interpretation: the infall is only clearly seen in the p- H_2O $2_{11}-2_{02}$ line (blue asymmetric profile).

5.4. Opacities and integrated line intensity ratios

Depending on whether the line is in absorption or in emission, two different methods are applied to derive the opacities. For the absorption lines, we estimate the opacities at the maximum of absorption from the line-to-continuum ratio in Tables 3-6 using

$$\tau = -\ln\left(\frac{T_{\text{mb}}}{T_{\text{cont}}}\right) \quad (1)$$

and assuming that the continuum is completely covered by the absorbing layer.

In all sources, even in central regions, all rare isotopologue lines are optically thin ($\tau < 1$). For the three sources (W43-MM1, DR21(OH), and NGC6334I(N)) exhibiting H_2^{17}O lines, the opacities are comparable, i.e. 0.11-0.17 and 0.04-0.1 for the $2_{12}-1_{01}$ and $1_{11}-0_{00}$ lines respectively. These opacities decrease from the less evolved (NGC6334I(N)) to the more evolved object (DR21(OH)). Interestingly, the $\text{H}_2^{18}\text{O}/\text{H}_2^{17}\text{O}$ opacity ratio for the $1_{11}-0_{00}$ line is close to the rare isotopologue ratio (4, see Sect. 6) for W43-MM1, while it is slightly different for the two other objects (2.7 ± 1.1 and 6.2 ± 2.8). Except for IRAS16272 ($\tau = 0.06$), the opacity of the p- H_2^{18}O $1_{11}-0_{00}$ line is around 0.3 for all sources, larger than what is estimated for the o- H_2^{18}O $1_{10}-1_{01}$ line (0.15-0.20) in W43-MM1 and NGC6334I(N).

In contrast, all the H_2^{16}O ground state lines in absorption are optically thick, even totally absorbed for the 1113 and 557 GHz lines. More generally, IRAS16272 is the source with the lower opacities while DR21(OH) has the highest opacity. The o- H_2O $2_{21}-2_{12}$ line is optically thin in the less evolved sources IRAS05358 and IRAS16272.

In order to study the excitation and physical conditions of the water-emitting gas, we now focus on the opacities of

the lines in emission. We first look for $\text{H}_2^{16}\text{O}/\text{H}_2^{18}\text{O}$ line pairs in our sample. Only the $3_{12} - 3_{03}$ line exhibits emission for both H_2^{16}O and H_2^{18}O (a blend of emission and absorption prevents us from any accurate comparison of other lines). This is only observed in IRAS05358, DR21(OH), and NGC6334I(N). We adopt the following standard abundance ratios (same ratios for all the lines): 4.5 for $\text{H}_2^{18}\text{O}/\text{H}_2^{17}\text{O}$ (Thomas & Fuller 2008), and 3 for ortho/para- H_2O . Based on Wilson & Rood (1994), the $^{16}\text{O}/^{18}\text{O}$ abundance ratio depends on the distance from the Galactic center (while the $\text{H}_2^{18}\text{O}/\text{H}_2^{17}\text{O}$ ratio is constant). From the Wilson and Rood results and the distance adopted for IRAS05358, IRAS16272, NGC6334I(N) and DR21(OH) (see Table 1) we derive an $\text{H}_2^{16}\text{O}/\text{H}_2^{18}\text{O}$ abundance ratio of 642, 363, 437 and 531, respectively. From the integrated intensity ratios for the $3_{12} - 3_{03}$ line, and assuming that both isotopes have the same excitation temperature, we estimate an optical depth of order 15-30 for the H_2^{16}O line, the H_2^{18}O line being optically thin (according to our models, see Sect. 6.1).

For sources or components for which H_2^{18}O data are not detected or usable, we follow the method described by Mottram et al. (2014). We use the ratio of the integrated intensity of the different components in pairs of H_2^{16}O lines which share a common level. In Table 7 we compare the ratios obtained for either the medium or broad component of the gas (again we restrict ourselves to the profiles with obvious components in emission) to the LTE ratios in the optically thin and thick regimes following Goldsmith & Langer (1999), for $T_{\text{ex}} = 300$ K like Mottram et al. (2014) (note that some of the line ratios values in Mottram's paper are incorrect and we have then corrected the ratios from those given in Mottram et al. to the values listed in Table 7), and also for $T_{\text{ex}} = 100$ and 500 K. The thin and thick line ratios for $T_{\text{ex}} = 300$ and 500 K differ by only 10% which is not significant compared to the observed ratios. Decreasing T_{ex} has a larger impact, but does not change the interpretation. The line ratios must be corrected by a factor reflecting the different beam sizes of the observations (θ_1/θ_2 , see Table 7). This correction factor is different depending on either the emission comes from a point source, $(\theta_1/\theta_2)^2$, fills the beam in one axis and is point-like in the other, θ_1/θ_2 , or if the emitting region covers both axes (no correction). For our high-mass objects (mainly because of the large distance), one can only assume that the broad component for the ground-state lines covers the beam (based on HIFI maps, see Jacq et al., in preparation) while the other line emission should be smaller than the beam. Hence, we will consider the cases θ_1/θ_2 and $(\theta_1/\theta_2)^2$. Intermediate cases apply if one line is optically thick but the other is optically thin, or if the transitions are sub-thermally excited at temperatures less than 300 K.

For the broad component, nearly all line ratios are close to the optically thick limit (after beam correction). IRAS05358 is a difficult case because the $1_{10} - 1_{01}/2_{12} - 1_{01}$ ratio is close to the optically thin limit, even considering the large difference in beam size and likely emitting regions. The thick case is probably valid for the $1_{11} - 0_{00}/2_{02} - 1_{11}$ ratio even if the beam correction factor is close to 1. Nevertheless, considering the high critical densities of these water transitions (see Table 2), these lines can be sub-thermally excited. The medium velocity component in IRAS05358 is obviously in the optically thick limit while the conclusion is uncertain for DR21(OH) and IRAS16272. Likely the LTE conditions do not apply to the medium component in these sources.

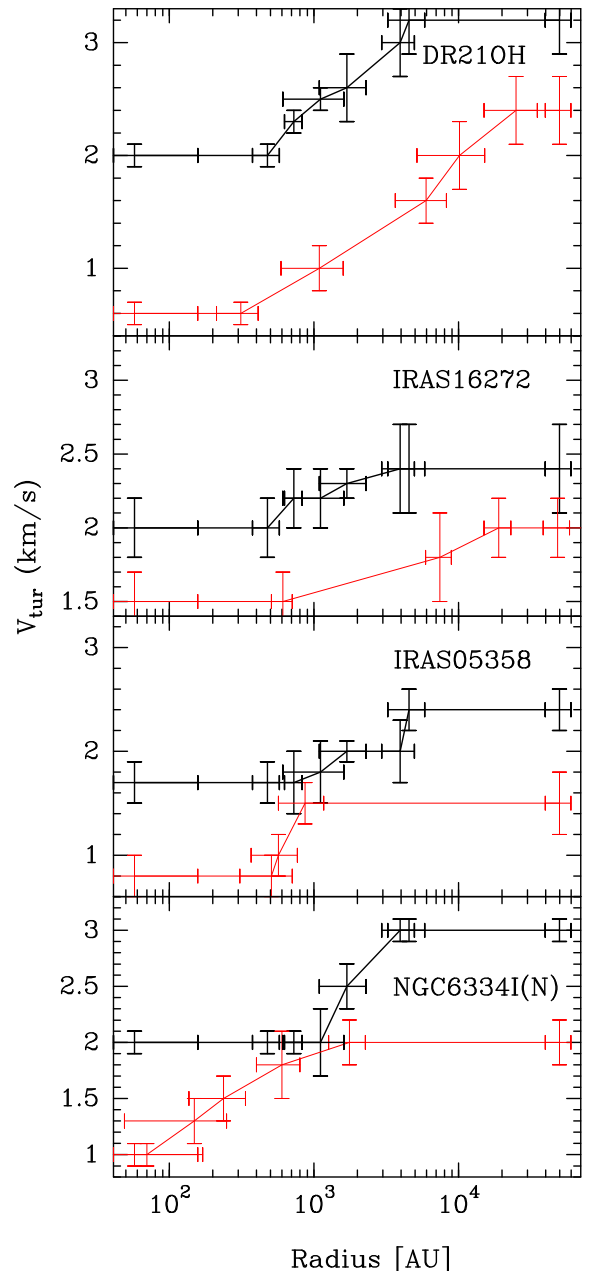


Fig. 7. Variation of the turbulent velocity V_{turb} with the distance R (AU) to the central object as derived from the model for water (in black) and CS (in red, see Appendix D). Error bars illustrate the range of values without any impact on the model.

6. Modeling

While the previous sections have presented the different velocity components in the observed lines profiles and indications of infall/expansion and outflow in the observed massive protostellar objects, this section intends to model the full line profiles in a single spherically symmetric model. The dynamics is driven by turbulence, infalling motions and outflow components.

6.1. Method

For all sources, the envelope temperature and density structure from van der Tak et al. (2013) are used as input to the 1D-radiative transfer code RATRAN (Hogerheijde & van der Tak 2000) in order to reproduce simultaneously all the water line

Table 8. Derived parameters from RATRAN model and accretion luminosities.

Object	χ_{out} 10 ⁻⁸	χ_{in} 10 ⁻⁵	M_{H_2O} [10 ⁻⁴ M _⊙]	M_{H_2O} [10 ⁻⁷ M _{env}]	M_{inner} [% M _{total}]	V_{inf} [km s ⁻¹]	$L_{tot}/(c.v_{inf})$ [M _⊙ .yr ⁻¹]	\dot{M}_{acc} [M _⊙ .yr ⁻¹]	L_{acc} [10 ³ L _⊙]
NGC6334I(N)	2.3	0.4	8.8	2.3	3.6	-0.7	5.4×10^{-5}	$5.2\text{-}5.6 \times 10^{-4}$	3.1-3.3
W43-MM1	6.7	14	1100	146	97.2	-2.9	1.6×10^{-4}	$3\text{-}4 \times 10^{-2}$	30
DR21(OH)	14	0.5	7.7	16.3	11.8	-1.5	1.7×10^{-4}	$9.6\text{-}11 \times 10^{-5}$	0.58-0.66
IRAS16272	4.7	0.17	1.3	0.6	43.8	-0.2	$2. \times 10^{-3}$	$6.3\text{-}6.8 \times 10^{-5}$	0.38-0.41
IRAS05358	8.8	1.3	1.1	7.7	26.7	+3.0	N/A	N/A	N/A

profiles, following the method of Herpin et al. (2012). The H₂O collisional rate coefficients are from Daniel et al. (2011).

As in our previous publications (i.e., Chavarría et al. 2010; Marseille et al. 2010b; Herpin et al. 2012), the source model has two gas components: an outflow and the proto-stellar envelope. The outflow parameters, intensity and width, come from the Gaussian fitting presented in Section 4. The envelope contribution is parametrized with three input variables: water abundance (χ_{H_2O}), turbulent velocity (V_{turb}), and infall velocity (V_{inf}). The width of the line is adjusted by varying V_{turb} . The line asymmetry is reproduced by adjusting the infall velocity parameter. The line intensity is best fitted by adjusting a combination of the abundance, turbulence, and outflow parameters. We adopt the abundance ratios presented in Sect. 5.4. The models assume a jump in the abundance in the inner envelope at 100 K (see Section 6.3) due to the evaporation of ice mantles. Table 8 gives the parameters used in the models.

Our modeling strategy consists in fitting first the rare isotopologue lines (H₂¹⁷O and H₂¹⁸O) since they are optically thin (see Sect. 5.4). Then we model the H₂¹⁶O lines starting from the highest energy level (the H₂¹⁶O abundances are derived from the H₂¹⁷O and H₂¹⁸O values times the isotopic abundance ratios). Once we are able to reproduce the main features of the profiles by minimizing the residuals (see Herpin et al. 2012) in a grid of values, we model the remaining lines using the same parameters, including the outflow component when this is justified.

6.2. Velocity structure

Thanks to the high spectral resolution HIFI observations, we have access to crucial velocity details as already explained in Sect. 4 which help to constrain the source dynamics. In W43-MM1 Herpin et al. (2012) have shown that a turbulence increasing with circumstellar radius provided the best line model. In order to test this conclusion in the other sample sources, we first try a model where turbulent velocity (and infall or expansion) is constant with radius for all lines, and then a model in which V_{turb} varies with radius. For the constant model, the best fitted V_{turb} values (same for all lines) are 2.5, 2.5, 2.2, and 2.0 km s⁻¹ (and V_{inf} as in Table 8) respectively for DR21(OH), NGC6334I(N), IRAS16272, and IRAS05358 (line models are in red in Fig. 2-5). Except for DR21(OH), the model with constant velocity parameters for all lines fits the H₂¹⁸O and H₂¹⁷O data quite well as it does for C¹⁸O (San José-García et al. 2013). In contrast, it is not possible to converge to a good model for all H₂¹⁶O lines, even though the line profiles of IRAS05358 and IRAS16272 are well reproduced.

Inspection of the line profiles (see Tables 3-6) shows that the width of the velocity components is not the same for all lines. As for W43-MM1 (Herpin et al. 2012) we do not expect a model with equal velocity parameters for all lines to fit the data well. Hence, as a second step we try a model in which the

turbulent velocity varies with radius. We have tested several possibilities: a power-law variation, then various step profiles based on the turbulent velocity estimated for each line from Tables 3-6). The best models are obtained using the turbulence profiles shown in black in Fig. 7 and overplotted in blue on Fig. 2-5. For IRAS16272, the adopted turbulent profile is quite flat and improvement of the model fit is small and significant only for the o-H₂O 1₁₀-1₀₁ and p-H₂O 2₀₂-1₁₁ lines. An increasing turbulent velocity in IRAS05358 gives a better result for at least the p-H₂O 2₁₁-2₀₂ and o-H₂O 3₁₂-3₀₃ lines, the other line profiles being less sensitive to this change. The two other sources, DR21(OH) and NGC6334I(N) are the most sensitive to the turbulent velocity profile. The relatively steep profiles leading to the best lines fitting vary from 2 up to at least 3 km s⁻¹ and strongly impact the depth and width of the absorption components (all isotopes). Clearly, a model in which the turbulent velocity increases with radius works better for NGC6334I(N), DR21(OH), and IRAS05358, whereas this is less clear for IRAS16272. Moreover, as explained in Appendix D, this also applies to the CS line modeling (see red plot in Fig. 7).

6.3. Abundance structure

The abundance is constrained by the modeling of the entire set of observed lines. Even if, as underlined by Herpin et al. (2012), only a couple of these lines (o-H₂¹⁸O 3₁₂-3₀₃ and o-H₂O 3₁₂-3₀₃) are optically thin enough to probe the inner part of the envelope, part of all water line profiles is produced by water excited in the inner part and is revealed by the high spectral resolution of these observations. Moreover, for DR21(OH) we have access to the high-excitation p-H₂O 5₂₄-4₃₁ line. In addition, we have applied our model to the H₂¹⁸O 3₁₃ - 2₂₀ line at 203.3916 GHz (E_{up} =204 K) observed toward IRAS05358 (not detected) and DR21(OH) by Marseille et al. (2010a). As illustrated by the analysis in Visser et al. (2013) for low-mass sources, the 203 GHz line is actually very useful because it is less optically thick due to lower Einstein A-coefficient and the dust continuum is more optically thin in the inner envelope, an issue that may certainly affect the high-mass sources. For these reasons, this sample of lines should probe the entire water region.

All line profiles are well reproduced. No deviation from the standard *o/p* ratio of 3 is found. The H₂¹⁶O abundances relative to H₂ (see Table 8) range from 1.7×10^{-6} (IRAS16272) to 1.3×10^{-5} (IRAS05358) in the inner part where $T > 100$ K while the outer abundances (where $T < 100$ K) are a few 10^{-8} (except DR21(OH), 1.4×10^{-7}). These abundances are typical of those found in HMPO's (e.g., Marseille et al. 2010b; Herpin et al. 2012). While the water outer abundance is close to the common values of a few 10^{-8} (Marseille et al. 2010b; Emprechtinger et al. 2013) for all sources, the relatively broad range of values ($1.7 \times 10^{-6} - 1.4 \times 10^{-4}$) derived for the inner abundance requires further discussion (see Sect. 7.1). Except for

W43-MM1, all our estimated inner water abundances are below the predicted high water inner abundance value from Fraser et al. (2001) (see Table 8).

From our RATRAN models and the physical structure adopted for our sources (van der Tak et al. 2013), we find that all inner abundances correspond to a region where $n_{H_2} \sim 1 - 4 \times 10^7 \text{ cm}^{-3}$ and $T_{dust} \sim 115 \text{ K}$ (except IRAS05358, 180 K) while the outer abundances are found for $n_{H_2} \sim 10^6 \text{ cm}^{-3}$ and $T_{dust} \sim 25 - 50 \text{ K}$. The region of the envelope probed by our observations is then roughly between 500 and 10000 AU. This also applies to W43-MM1 ($n_{H_2} \sim 4 \times 10^7 / 10^6 \text{ cm}^{-3}$ and $T_{dust} \sim 210/30 \text{ K}$) where the largest inner abundance is observed. This range of distances is exactly where the turbulent velocity is increasing in our model (see Sect.6.2). We stress that our Ratran modeling is 1D only so the inferred distance is just indicative. Also we assume perfect symmetry which of course is questionable in massive objects.

Schmalzl et al. (2014) have used a small (N reactions) chemical network (SWaN) to predict realistic water abundance profiles for low-mass protostellar envelopes, which have significantly improved the HIFI water line modeling for low-mass protostellar cores. Applying this chemistry network to our high-mass protostellar objects is very difficult because several crucial input parameters are not well known or are not optimized for high-mass protostars (e.g. the large amounts of UV photons produced by the massive object). Moreover, a large range of parameters has to be explored in order to get a realistic model. Even if the abundance profile is then only illustrative, we have used SWaN with one single set of input parameters only for IRAS05358 in order to illustrate that the outer abundance varying with radius likely affects the line profiles. The output of the line modeling is shown in green on Fig.5. The result is worse than with a step-profile but has a clear impact on some line profiles.

7. Discussion

7.1. Why do the inner envelopes appear so dry?

Compared to previous studies of the water content in HM protostars (e.g. Boonman et al. 2003), HIFI gives us access to multiple water lines, and, hence, enables us to model the complete water spectra in a robust and quite self-consistent way. Moreover, the use of resolved spectral lines allows us to separate the various kinematic components, and thus to partly compensate for the lack of spatial resolution. Our line sample probes deep enough the inner envelope at least for DR21(OH), IRAS05358, and W43-MM1 where we include in our model the $3_{13}-2_{20}$ transition of $H_2^{18}O$ (which strongly constrains the inner water abundance as explained in Sect. 6.3). On the other hand, we adopt here a simplified physical model, which is only constrained by single dish dust continuum data, hence not sensitive to physical structure of the hot inner core, whereas a highly complex structure is known for most of the studied sources (e.g. Zapata et al. 2012). Hence the high outer (1.4×10^{-7}) and low inner (5×10^{-6}) abundances derived for instance for DR21(OH) do not exclude the presence of a warm inner region which is not well reproduced in our model. At the studied scale, according to the literature the same argument can be hardly applied to the other sources. Recent work by Visser et al. (2013) shows that in low-mass objects the spherical geometry as adopted here is not valid on the spatial scale of the hot core: a spherical envelope model with a single power-law density profile might lead to underestimate the inner water abundance. Obviously further investigation with more realistic physical model is necessary. From the observational side,

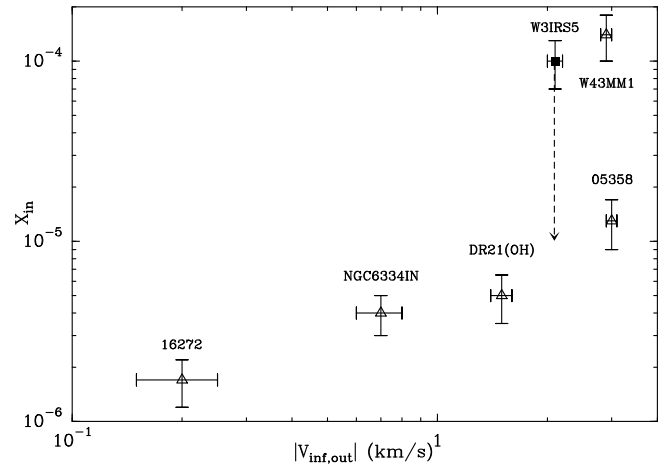


Fig. 8. Inner water abundance vs. the absolute value of the infall or expansion velocity as derived from our model (see Table 8). The filled square symbol is for W3IRS5 from Chavarría et al. (2010), and the arrow shows the abundance for W3IRS5 from van der Tak et al. (2006).

the need for high spatial resolution observation has been well shown by van der Tak et al. (2006) in order to get a precise estimate of the water inner abundance. Therefore further confirmation of our results by interferometric ALMA or NOEMA observations have to be done.

We have searched for a possible relation between kinematics and water abundances. First we investigate if a high level of turbulence could enhance (e.g. through shocks) the inner water abundance. No correlation is found between χ_{in} and the turbulent velocity ($V_{turb-min}$, $V_{turb-max}$, or $\overline{V_{turb}}$), or the outflow velocity (see Tables 3-6, 8, and Fig. 7). On the other hand, the higher the infall/expansion velocity ($|V_{inf,out}|$) is, the higher the inner abundance (see Fig. 8). Adding the W3IRS5 result (10^{-4}) from Chavarría et al. (2010) confirms this trend. The trend is even strengthened if we rather use the estimate ($\sim 10^{-5}$) from van der Tak et al. (2006) and Choi et al. (in preparation) for this source. Combined with the large turbulence observed in the high-mass protostellar objects, we propose that larger infall/expansion velocities generate shocks that will sputter water out of the dust grain mantles. Nevertheless according to Neufeld et al. (2014) shock velocities of $\sim 20 - 25 \text{ km s}^{-1}$ are necessary to release water from ice mantles.

Another explanation to the low inner abundance could be that photodissociation through protostellar UV photons is more efficient than expected and thus not completely outrun by the $O \rightarrow H_2O$ conversion. In the presence of strong UV radiation fields like the internal extreme UV radiation from the surface of a massive star (e.g. $3 \times 10^{38} \text{ erg.s}^{-1}$, Benz et al. 2013), water vapor is photodissociated. The physical known characteristics of our sources (see Table 1) do not indicate any difference in terms of FUV internal field among our sample, but we can imagine that for some reasons (e.g. self-shielding due to the thickness of the inner region) water photodissociation is more efficient in IRAS16272 than in W43-MM1 for instance. Observing good FUV irradiation tracers such as OH^+ or CH^+ , or the product of the water photodissociation, i.e. OH , could help to constrain this scenario.

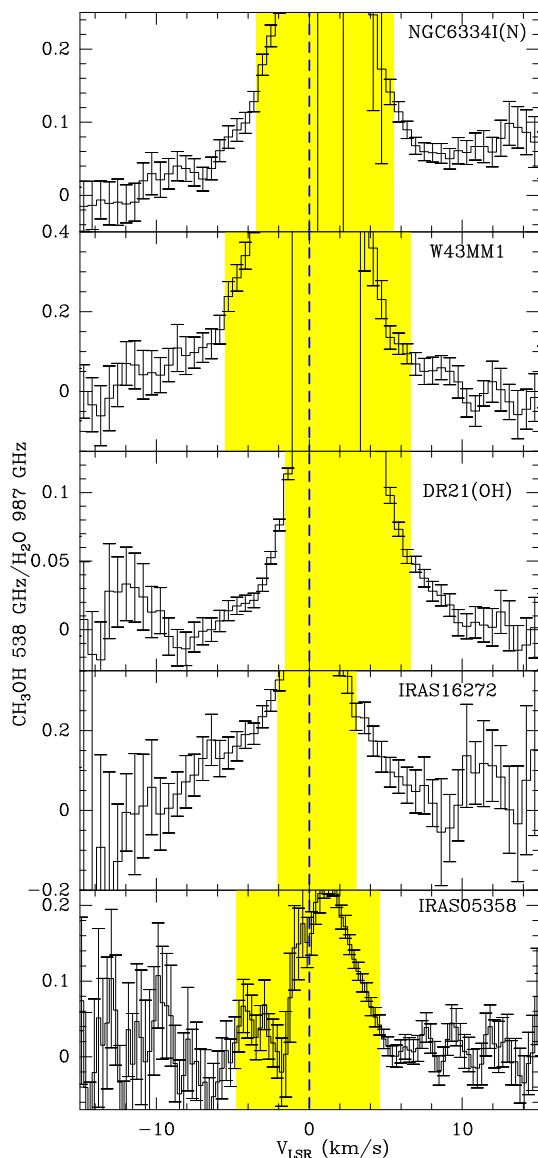


Fig. 9. Line ratio of the $\text{CH}_3\text{OH } 5_{1,5} - 4_{0,4} A_+ - A_+$ over the $\text{p-H}_2\text{O } 2_{02}-1_{11}$ transition, both rebinned to 0.5 km s^{-1} . The V_{LSR} is shown with a dashed line. The range of velocities where the high optical depth of the water is assumed to affect the derived ratio is shown in yellow.

7.2. Methanol and the formation route of water at higher velocities

Among the various species detected in our spectra (see Tables B.1-B.5), methanol lines, because of their large number, are important indicators of the physical conditions in the protostellar envelope. The observed line ratio of CH_3OH over water as a function of the velocity in the line wings is able to differentiate between two potential formation routes of H_2O , gas-phase synthesis versus a sputtered origin in the outflow (Suutarinen et al. 2014). van Kempen et al. (2014) have shown that in intermediate-mass protostars organic molecules (e.g. the pure grain mantle product CH_3OH) likely originate from sputtering of ices due to outflow shocks and cannot form through gas-phase synthesis, as opposed to H_2O . Contrary to the water lines, most of the CH_3OH lines detected in our sample do not exhibit a broad component, but rather a medium velocity component. Hence, comparison of water and CH_3OH velocity components (e.g., see Fig. B.4) shows that methanol does not trace

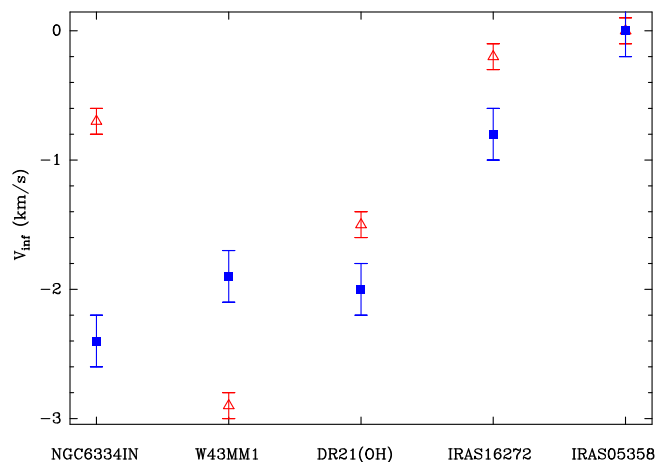


Fig. 10. Infall velocity vs. evolutionary sequence. Red triangles and filled blue squares represent respectively H_2O and CS (see Appendix D) velocities.

exactly the same gas as the water broad component, or that the abundance ratio is much smaller in the shocks. Among the detected methanol lines with a good S/N, we have compared the CH_3OH lines whose upper energy level is comparable ($E_u \leq 105 \text{ K}$, $5_{1,5} - 4_{0,4} A_+ - A_+$, $6_{3,4} - 5_{2,3} A_+ - A_+$, $6_{3,3} - 5_{2,4} A_- - A_-$, and $8_{1,7} - 7_{0,7} E$) with the $\text{p-H}_2\text{O } 2_{02}-1_{11}$ line. All transitions are assumed to fill the beam. Following van Kempen et al. (2014), we do not consider a range of velocities around the line center where significant optical depth in the water lines increases the line ratio much more than physical processes would do. As explained in Sect. 5.4, considering the high critical densities of water transitions, we will assume effectively thin emission away from this central line region (according to Suutarinen et al. 2014, the effect of water opacity on the ratio is still small).

Figure 9 shows the ratio for the $\text{CH}_3\text{OH } 5_{1,5} - 4_{0,4} A_+ - A_+$ over the $\text{p-H}_2\text{O } 2_{02}-1_{11}$ transitions. Except for IRAS05358 where the methanol line does not show any wing, the ratio clearly drops as a function of velocity on both wings (although the number of channels in the red wing not affected by optical depth is smaller), suggesting, since methanol is produced on grain surfaces, a dominant gas-phase synthesis of H_2O from shocked material. Line ratios of other CH_3OH lines over the same H_2O line (or $\text{p-H}_2\text{O } 2_{11}-2_{02}$) show the same behavior. We can hence conclude that high-velocity water must be formed in the gas-phase from shocked material, i.e. not created solely through grain mantle evaporation.

7.3. Star formation processes and evolution

Turbulence, infall, and outflow are important ingredients of the star formation process. We confirm here that the observed molecular emission in massive protostellar objects is dominated by supersonic turbulent velocities (see Fig. 7) at all radii. Hence regions of massive-star formation are highly turbulent. This supersonic turbulence is in agreement with the turbulent core model of McKee & Tan (2003), but is also consistent with the competitive accretion scenario in which local velocity dispersions are small but line-of-sight ones can be significantly larger due to the fragmentation of the cloud (Bonnell & Bate 2006). Moreover, our results indicate that the turbulent motions tend to increase with radius, consistent again with all models (see Bonnell & Bate 2006; McKee & Tan 2003). Nevertheless, rotation and non-spherical density structure cannot be excluded as possible explanations

Table 9. Observed fluxes and luminosities for all lines and sources.

Line	NGC6334I(N)		DR21(OH)		IRAS16272		IRAS05358	
	F [10 ⁻²¹ W.cm ⁻²]	L _⊙ [10 ⁻²]	F [10 ⁻²¹ W.cm ⁻²]	L _⊙ [10 ⁻²]	F [10 ⁻²¹ W.cm ⁻²]	L _⊙ [10 ⁻²]	F [10 ⁻²¹ W.cm ⁻²]	L _⊙ [10 ⁻²]
H₂¹⁸O								
1 ₁₀ -1 ₀₁			1.7(0.2)	0.12(0.02)	0.2(0.1)	0.07(0.04)		
2 ₀₂ -1 ₁₁			5.7(0.6)	0.40(0.04)				
3 ₁₂ -3 ₀₃	0.4(0.2)	0.04(0.02)	4.1(0.4)	0.29(0.03)			0.8(0.2)	0.08(0.02)
1 ₁₁ -0 ₀₀			1.4(0.2)	0.10(0.02)				
H₂¹⁷O								
1 ₁₀ -1 ₀₁			0.8(0.6)	0.05(0.04)				
1 ₁₁ -0 ₀₀			2.1(0.3)	0.15(0.02)				
H₂O								
1 ₁₀ -1 ₀₁	20(2)	1.8(0.2)	28(1)	1.97(0.07)	5.8(0.3)	2.1(0.1)	5.6(0.7)	0.57(0.07)
2 ₁₁ -2 ₀₂	49(2)	4.4(0.2)	74(5)	5.2(0.4)	17.4(0.8)	6.3(0.3)	15.5(0.8)	1.57(0.08)
5 ₂₄ -4 ₃₁			2.7(0.7)	0.19(0.05)				
2 ₀₂ -1 ₁₁	60(4)	5.4(0.4)	108(6)	7.6(0.4)	19(1)	6.9(0.4)	37(1)	3.7(0.1)
3 ₁₂ -3 ₀₃	34(2)	3.1(0.2)	87(6)	6.1(0.4)	15(1)	5.4(0.4)	28(1)	2.8(0.1)
1 ₁₁ -0 ₀₀	23(2)	2.1(0.2)	42(5)	3.0(0.4)	8.9(0.6)	3.2(0.2)	23(1)	2.3(0.1)
2 ₂₁ -2 ₁₂							14(4)	1.4(0.4)
2 ₁₂ -1 ₀₁			120(20)	8(1)			20(4)	2.0(0.4)

(see Herpin et al. 2012) and accurate estimates of the turbulence also require careful subtraction of cold foreground clouds in some cases (Jacq et al in prep).

Assuming isotropic radiation, from the integrated fluxes of components in emission in observed lines (Table 9), we estimate the lower limit to the total HIFI water luminosity by adding all individual observed luminosities to be 16.8, 33.1, 23.9, and 14.4 L_⊙ in our sources (evolutionary order). This confirms the low contribution of water cooling to the total far-IR gas cooling compared to the cooling from other species (Karska et al. 2014). The true water emission from the inner part could be much larger but the cool envelope absorbs much of the emission. Moreover, from the modeling we estimate the total water mass in the envelope (see Table 8) to roughly $8 - 9 \times 10^{-4} M_{\odot}$ for NGC6334I(N) and DR21(OH), and $10^{-4} M_{\odot}$ for the two other objects. The fraction of the water mass to the envelope mass differs by more than an order of magnitude from source to source (0.6×10^{-7} to 16.3×10^{-7}). The proportion of the mass in the inner part is only 3.6% for NGC6334I(N) and 11.8% for DR21(OH), but increases to 26.7% and 43.8% respectively for the more evolved object IRAS05358 and IRAS16272.

If the whole envelope mass (see Table 1) would be collapsing, assuming free-fall accretion one would expect infall velocities from 2.1 km s⁻¹ for IRAS05358 up to 9.7 km s⁻¹ for NGC6334I(N), larger by up to a factor of 10 than what we estimate here (we even detect no infall in IRAS05358 consistent with HCO⁺ observations of Klaassen et al. 2012). The free-fall accretion rate (monolithic collapse, Shu 1977) is $6.3 \times 10^{-6} M_{\odot}/\text{yr}$ for sound speed of 0.3 km s⁻¹ (a few $10^{-5} M_{\odot}/\text{yr}$ for temperatures above 100 K), hence several orders of magnitude smaller than what we derived from our observations (see Table 8). We note that the CS infall velocity provides us with another estimate of the mass accretion rate (see Table D.1 in Appendix D), approximately 50% lower than the values inferred from the water lines. Models of star formation based on gravoturbulent fragmentation (Schmeja & Klessen 2004) predict mass accretion rates of $3.4 \times 10^{-5} M_{\odot}/\text{yr}$ (same sound speed of gas) but varying with time, while this rate is constant in the standard theory of isolated star formation from Shu (1977). Of course, these accretion rates from our calculations assume spherical accretion and one central object, which is likely not true. Nevertheless,

these rates are comparable to those derived from the turbulent core model for massive molecular cloud cores dominated by supersonic turbulence (a few $10^{-5} - 10^{-4} M_{\odot}/\text{yr}$, McKee & Tan 2003) and from the competitive accretion model which can produce accretion rates from 10^{-9} to $10^{-4} M_{\odot}/\text{yr}$ (depending on the gas density and initial stellar, fragment, mass). Models of gravitational collapse of massive magnetized molecular cloud cores (e.g., Banerjee & Pudritz 2007) generate massive star formation via high accretion rates (that can exceed $10^{-3} M_{\odot}/\text{yr}$) and disk-driven outflows.

Considering a typical mass of 20 M_{\odot} within a radius of 100 R_★, we estimate the corresponding accretion luminosity of a protostar from Hosokawa et al. (2010) using

$$L_{\text{acc}} = G \frac{M_{\star} \dot{M}_{\text{acc}}}{R_{\star}} \quad (2)$$

The derived luminosities (see Table 8), compared to the observed total luminosity (stellar+accretion, Table 1) seem unrealistically high for W43-MM1 and NGC6334I(N), but we stress that the scales of infall probed by water and the accretion onto the protostars are likely quite different: what we probe here is infall in the envelope rather than accretion onto the protostar. However, using the lower values derived from CS observations, the accretion luminosities are compatible with the observed total luminosity, so we suggest that water may not be a good accretion tracer. Moreover, the derived accretion rate, although uncertain, is high enough for W43-MM1 and NGC6334I(N) to overcome the radiation pressure due to the stellar luminosity (see Table 9). This is possibly true for DR21(OH) too, but not for IRAS16272 (no accretion is detected in IRAS05358). Nevertheless, the simple comparison of radiation pressure and mass accretion rate in the simple one-dimensional collapse model view is considered as insufficient to explain the observations (Peters et al. 2010).

Beyond the classical monolithic collapse and competitive accretion model, Peters et al. (2010) proposed the collapse of a rotating massive cloud core involving a process called fragmentation-induced starvation to reproduce the strong clumping and filamentary structures observed in collapsing cores. According to this model, the accretion is decreasing with time (between 10^{-3} and $10^{-5} M_{\odot}/\text{yr}$), consistent with results from Peters et al. (2010). But considering the evolutionary sequence

described in Sect. 3, the accretion rates derived for our sample (Table 8) do not show any trend.

Because of the different level of fragmentation/substructure in our source sample, comparing estimates of the mass accretion rates along the evolutionary sequence of this sample is uncertain. Nevertheless, the infall velocity derived from H₂O (except for NGC6334IN) and CS observations tends to decrease with the evolutionary stage of the massive object (Fig.10).

8. Conclusions

We have presented Herschel-HIFI observations of 14 far-IR water lines (H₂¹⁶O, H₂¹⁷O, H₂¹⁸O) toward four mid-IR quiet massive protostellar objects, assumed to be at the beginning of the high-mass star formation process, and ordered in terms of an evolutionary sequence based on their SED. We have studied the envelope kinematics (outflow, infall, turbulent velocity) from the different components identified in the line profiles of our source sample, and we have derived the water abundances using the RATRAN radiative transfer code. In addition, our analysis has been supplemented in terms of 'evolution' and water formation by the serendipitous detection of several other molecular lines, especially CS and methanol.

The water lines have broad, medium, and narrow velocity components while no envelope component was found in W43-MM1 by Herpin et al. (2012). The more evolved sources, IRAS05358 and IRAS16272, exhibit fewer and weaker rare isotopologue lines and appear to be less rich chemically as indicated by the number of serendipitous species detected in these observations. We confirm that regions of massive star formation are highly turbulent and that turbulence tends to increase in the envelope with the distance to the star, as seen in W43-MM1 by Herpin et al. (2012). This trend is consistent with the supersonic turbulent core model leading to high mass star formation in the presence of a disk, although these constraints are also consistent with competitive accretion.

The whole set of lines allowed us to constrain by modeling the outer water abundance to the typical value of a few 10^{-8} while we infer $1.7 \times 10^{-6} - 1.4 \times 10^{-4}$ for the inner abundance, lower (except for W43-MM1) than expected from ice evaporation. Possible explanations could be : (i) Photodissociation of water from the massive protostar UV internal photons is more efficient than expected, or (ii) Our simple spherical envelope model underestimates the inner water abundance. Moreover, we show that the higher the infall/expansion velocity in the protostellar envelope, the higher is the inner abundance. This fact, in addition to the observed lower infall velocity along the source evolutionary sequence, suggests that the younger sources with larger infall/expansion velocities may generate shocks that will sputter water from the ice mantles of dust grains in the inner region. At high velocities, water must be formed in the gas-phase from shocked material, i.e. not created solely through grain mantle evaporation.

Acknowledgements. This program was made possible thanks to the HIFI guaranteed time. HIFI has been designed and built by a consortium of institutes and university departments from across Europe, Canada and the United States under the leadership of SRON Netherlands Institute for Space Research, Groningen, The Netherlands and with major contributions from Germany, France and the US. Consortium members are: Canada: CSA, U. Waterloo; France: CESR, LAB, LERMA, IRAM; Germany: KOSMA, MPIfR, MPS; Ireland, NUI Maynooth; Italy: ASI, IFSI-INAf, Osservatorio Astrofisico di Arcetri- INAF; Netherlands: SRON, TUD; Poland: CAMK, CBK; Spain: Observatorio Astronómico Nacional (IGN), Centro de Astrobiología (CSIC-INTA). Sweden: Chalmers University of Technology - MC2, RSS & GARD; Onsala Space Observatory; Swedish National Space Board, Stockholm University - Stockholm Observatory; Switzerland: ETH Zurich, FHNW; USA: Caltech, JPL, NHSC. HIPE is a joint develop-

ment by the Herschel Science Ground Segment Consortium, consisting of ESA, the NASA Herschel Science Center, and the HIFI, PACS and SPIRE consortia. Astrochemistry in Leiden is supported by the Netherlands Research School for Astronomy (NOVA), by a Spinoza grant and grant 614.001.008 from the Netherlands Organisation for Scientific Research (NWO), and by the European Community's Seventh Framework Program FP7/2007-2013 under grant agreement 238258 (LASSIE). We also thank the French Space Agency CNES for financial support. We thank J. Mottram for useful comments and discussions.

References

- Aikawa, Y., Wakelam, V., Garrod, R. T., & Herbst, E. 2008, *ApJ*, 674, 984
- Araya, E. D., Kurtz, S., Hofner, P., & Linz, H. 2009, *ApJ*, 698, 1321
- Banerjee, R. & Pudritz, R. E. 2007, *ApJ*, 660, 479
- Benz, A. O., Bruderer, S., van Dishoeck, E. F., Stäuber, P., & Wampfler, S. F. 2013, *Journal of Physical Chemistry A*, 117, 9840
- Benz, A. O., Bruderer, S., van Dishoeck, E. F., WISH Team, & HIFI Team. 2010, *ArXiv e-prints*
- Beuther, H., Leurini, S., Schilke, P., et al. 2007, *A&A*, 466, 1065
- Beuther, H., Schilke, P., Gueth, F., et al. 2002a, *A&A*, 387, 931
- Beuther, H., Schilke, P., Menten, K. M., et al. 2002b, *ApJ*, 566, 945
- Beuther, H., Walsh, A. J., Thorwirth, S., et al. 2008, *A&A*, 481, 169
- Bonnell, I. A. & Bate, M. R. 2006, *MNRAS*, 370, 488
- Bontemps, S., Andre, P., Terebey, S., & Cabrit, S. 1996, *A&A*, 311, 858
- Boonman, A. M. S., Doty, S. D., van Dishoeck, E. F., et al. 2003, *A&A*, 406, 937
- Brogan, C. L., Hunter, T. R., Cyganowski, C. J., et al. 2009, *ApJ*, 707, 1
- Bruderer, S., Benz, A. O., van Dishoeck, E. F., et al. 2010, *ArXiv e-prints*
- Ceccarelli, C., Bacmann, A., Boogert, A., et al. 2010, *A&A*, 521, L22
- Chandler, C. J., Moore, T. J. T., Mountain, C. M., & Yamashita, T. 1993, *MNRAS*, 261, 694
- Charney, S. B. 1997, *ApJ*, 481, 396
- Chavarría, L., Herpin, F., Jacq, T., et al. 2010, *A&A*, 521, L37+
- Cortés, P. C. 2011, *ApJ*, 743, 194
- Csengeri, T., Bontemps, S., Schneider, N., et al. 2011, *ApJ*, 740, L5
- Daniel, F., Dubernet, M.-L., & Grosjean, A. 2011, *A&A*, 536, A76
- de Graauw, T., Helmich, F. P., Phillips, T. G., et al. 2010, *A&A*, 518, L6+
- Emprechtinger, M., Lis, D. C., Rolfs, R., et al. 2013, *ApJ*, 765, 61
- Faúndez, S., Bronfman, L., Garay, G., et al. 2004, *A&A*, 426, 97
- Fraser, H. J., Collings, M. P., McCoustra, M. R. S., & Williams, D. A. 2001, *MNRAS*, 327, 1165
- Fuller, G. A., Williams, S. J., & Sridharan, T. K. 2005, *A&A*, 442, 949
- Garay, G., Mardones, D., Brooks, K. J., Videla, L., & Contreras, Y. 2007, *ApJ*, 666, 309
- Gerner, T., Beuther, H., Semenov, D., et al. 2014, *A&A*, 563, A97
- Girart, J. M., Frau, P., Zhang, Q., et al. 2013, *ApJ*, 772, 69
- Goldsmith, P. F. & Langer, W. D. 1999, *ApJ*, 517, 209
- Harvey, P. M., Joy, M., Lester, D. F., & Wilking, B. A. 1986, *ApJ*, 300, 737
- Heitsch, F., Hartmann, L. W., Slyz, A. D., Devriendt, J. E. G., & Burkert, A. 2008, *ApJ*, 674, 316
- Helmich, F. P., van Dishoeck, E. F., Black, J. H., et al. 1996, *A&A*, 315, L173
- Hennemann, M., Motte, F., Schneider, N., et al. 2012, *A&A*, 543, L3
- Herpin, F., Chavarría, L., van der Tak, F., et al. 2012, *A&A*, 542, A76
- Herpin, F., Marseille, M., Wakelam, V., Bontemps, S., & Lis, D. C. 2009, *A&A*, 504, 853
- Hogerheijde, M. R. & van der Tak, F. F. S. 2000, *A&A*, 362, 697
- Hosokawa, T., Yorke, H. W., & Omukai, K. 2010, *ApJ*, 721, 478
- Hunter, T. R., Brogan, C. L., Cyganowski, C. J., & Young, K. H. 2014, *ApJ*, 788, 187
- Hunter, T. R., Brogan, C. L., Megeath, S. T., et al. 2006, *ApJ*, 649, 888
- Jacq, T., Walmsley, C. M., Henkel, C., et al. 1990, *A&A*, 228, 447
- Johnstone, D., Fich, M., McCoe, C., et al. 2010, *A&A*, 521, L41+
- Karska, A., Herpin, F., Bruderer, S., et al. 2014, *A&A*, 562, A45
- Kaźmierczak-Barthel, M., Semenov, D. A., van der Tak, F. F. S., Chavarría, L., & van der Wiel, M. H. D. 2015, *A&A*, 574, A71
- Klaassen, P. D., Testi, L., & Beuther, H. 2012, *A&A*, 538, A140
- Kristensen, L. E., Visser, R., van Dishoeck, E. F., et al. 2010, *A&A*, 521, L30+
- Krumholz, M. R. & Bonnell, I. A. 2009, *Models for the formation of massive stars*, ed. Chabrier, G. (Cambridge University Press), 288
- Krumholz, M. R., McKee, C. F., & Klein, R. I. 2005, *ApJ*, 618, L33
- Kuiper, R., Klahr, H., Beuther, H., & Henning, T. 2010, *ApJ*, 722, 1556
- Kuiper, R., Yorke, H. W., & Turner, N. J. 2015, *ApJ*, 800, 86
- Lester, D. F., Dinerstein, H. L., Werner, M. W., et al. 1985, *ApJ*, 296, 565
- Leurini, S., Beuther, H., Schilke, P., et al. 2007, *A&A*, 475, 925
- Marseille, M. G., van der Tak, F. F. S., Herpin, F., & Jacq, T. 2010a, *A&A*, 522, A40+
- Marseille, M. G., van der Tak, F. F. S., Herpin, F., et al. 2010b, *A&A*, 521, L32+
- McCutcheon, W. H., Sandell, G., Matthews, H. E., et al. 2000, *MNRAS*, 316, 152

- McKee, C. F. & Tan, J. C. 2003, *ApJ*, 585, 850
- Motte, F., Bontemps, S., Schilke, P., et al. 2007, *A&A*, 476, 1243
- Motte, F., Schilke, P., & Lis, D. C. 2003, *ApJ*, 582, 277
- Mottram, J. C., Hoare, M. G., Davies, B., et al. 2011, *ApJ*, 730, L33+
- Mottram, J. C., Kristensen, L. E., van Dishoeck, E. F., et al. 2014, *A&A*, 572, A21
- Muñoz, D. J., Mardones, D., Garay, G., et al. 2007, *ApJ*, 668, 906
- Neufeld, D. A., Gusdorf, A., Güsten, R., et al. 2014, *ApJ*, 781, 102
- Ott, S. 2010, in *Astronomical Society of the Pacific Conference Series*, Vol. 434, *Astronomical Data Analysis Software and Systems XIX*, ed. Y. Mizumoto, K.-I. Morita, & M. Ohishi, 139–+
- Palau, A., Estalella, R., Girart, J. M., et al. 2014, *ApJ*, 785, 42
- Pearson, J. C., De Lucia, F. C., Anderson, T., Herbst, E., & Helminger, P. 1991, *ApJ*, 379, L41
- Peters, T., Klessen, R. S., Mac Low, M.-M., & Banerjee, R. 2010, *ApJ*, 725, 134
- Pilbratt, G. L., Riedinger, J. R., Passvogel, T., et al. 2010, *A&A*, 518, L1+
- Ragan, S., Henning, T., Krause, O., et al. 2012, *A&A*, 547, A49
- Richardson, K. J., Sandell, G., Cunningham, C. T., & Davies, S. R. 1994, *A&A*, 286, 555
- Roberts, J. F., Rawlings, J. M. C., & Stace, H. A. 2010, *MNRAS*, 408, 2426
- Rodríguez, L. F., Zapata, L. A., & Ho, P. T. P. 2007, *ApJ*, 654, L143
- Roelfsema, P. R., Helmich, F. P., Teyssier, D., et al. 2012, *A&A*, 537, A17
- San José-García, I., Mottram, J. C., Kristensen, L. E., et al. 2013, *A&A*, 553, A125
- San Jose-Garcia, I., Mottram, J. C., van Dishoeck, E. F., et al. 2015, *ArXiv e-prints*
- Sandell, G. 2000, *A&A*, 358, 242
- Schlingman, W. M., Shirley, Y. L., Schenk, D. E., et al. 2011, *ApJS*, 195, 14
- Schmalzl, M., Visser, R., Walsh, C., et al. 2014, *A&A*, 572, A81
- Schmeja, S. & Klessen, R. S. 2004, *A&A*, 419, 405
- Shipman, R. F., van der Tak, F. F. S., Wyrowski, F., Herpin, F., & Frieswijk, W. 2014, *A&A*, 570, A51
- Shirley, Y. L., Evans, II, N. J., Young, K. E., Knez, C., & Jaffe, D. T. 2003, *ApJS*, 149, 375
- Shu, F. H. 1977, *ApJ*, 214, 488
- Snell, R. L., Howe, J. E., Ashby, M. L. N., et al. 2000, *ApJ*, 539, L101
- Suutarinen, A. N., Kristensen, L. E., Mottram, J. C., Fraser, H. J., & van Dishoeck, E. F. 2014, *MNRAS*, 440, 1844
- Tan, J. C., Beltrán, M. T., Caselli, P., et al. 2014, *Protostars and Planets VI*, 149
- Tan, J. C. & McKee, C. F. 2002, in *Astronomical Society of the Pacific Conference Series*, Vol. 267, *Hot Star Workshop III: The Earliest Phases of Massive Star Birth*, ed. P. Crowther, 267–+
- Thomas, H. S. & Fuller, G. A. 2008, *A&A*, 479, 751
- Vallée, J. P. & Fiege, J. D. 2006, *ApJ*, 636, 332
- van der Tak, F. F. S., Black, J. H., Schöier, F. L., Jansen, D. J., & van Dishoeck, E. F. 2007, *A&A*, 468, 627
- van der Tak, F. F. S., Chavarría, L., Herpin, F., et al. 2013, *A&A*, 554, A83
- van der Tak, F. F. S., Marseille, M. G., Herpin, F., et al. 2010, *A&A*, 518, L107+
- van der Tak, F. F. S., van Dishoeck, E. F., Evans, II, N. J., & Blake, G. A. 2000, *ApJ*, 537, 283
- van der Tak, F. F. S., Walmsley, C. M., Herpin, F., & Ceccarelli, C. 2006, *A&A*, 447, 1011
- van der Wiel, M. H. D., Pagani, L., van der Tak, F. F. S., Kaźmierczak, M., & Ceccarelli, C. 2013, *A&A*, 553, A11
- van Dishoeck, E. F. & Helmich, F. P. 1996, *A&A*, 315, L177
- van Dishoeck, E. F., Herbst, E., & Neufeld, D. A. 2013, *Chemical Reviews*, 113, 9043
- van Dishoeck, E. F., Kristensen, L. E., Benz, A. O., et al. 2011, *PASP*, 123, 138
- van Kempen, T. A., McCoey, C., Tisi, S., Johnstone, D., & Fich, M. 2014, *A&A*, 569, A53
- Vázquez-Semadeni, E., Gómez, G. C., Jappsen, A. K., et al. 2007, *ApJ*, 657, 870
- Villanueva, G. L., DiSanti, M. A., Mumma, M. J., & Xu, L.-H. 2012, *ApJ*, 747, 37
- Visser, R., Jørgensen, J. K., Kristensen, L. E., van Dishoeck, E. F., & Bergin, E. A. 2013, *ApJ*, 769, 19
- Walsh, A. J., Burton, M. G., Hyland, A. R., & Robinson, G. 1998, *MNRAS*, 301, 640
- Wilson, T. L. & Rood, R. 1994, *ARA&A*, 32, 191
- Woody, D. P., Scott, S. L., Scoville, N. Z., et al. 1989, *ApJ*, 337, L41
- Wu, J., Evans, II, N. J., Shirley, Y. L., & Knez, C. 2010, *ApJS*, 188, 313
- Wyrowski, F., van der Tak, F., Herpin, F., et al. 2010, *A&A*, 521, L34
- Yorke, H. W. & Sonnhalter, C. 2002, *ApJ*, 569, 846
- Zapata, L. A., Loinard, L., Su, Y.-N., et al. 2012, *ApJ*, 744, 86
- Zinnecker, H. & Yorke, H. W. 2007, *ARA&A*, 45, 481

Appendix A: AOR list**Appendix B: By-product lines****Appendix C: Gaussian fit components for IRAS05358****Appendix D: CS distribution**

We have also applied the model to the CS 11-10 line. In addition we tried to reproduce other CS lines observed by other authors: J=7-6 for W43-MM1 (Herpin et al. 2009) and NGC6334I(N) (McCutcheon et al. 2000), J=5-4 for IRAS05358 and W43-MM1 (Herpin et al. 2009), DR21(OH) (Richardson et al. 1994), J=3-2 for IRAS05358 (Herpin et al. 2009), and J=2-1 for IRAS16272 (Mopra observation, Herpin et al., unpublished). Hence, the sources IRAS05358 and W43-MM1 are the best constrained due to the number of CS lines available. Results for CS 11-10 line are shown on Fig.B.2. For all sources but DR21(OH), a jump of abundance is necessary to reproduce the lower-J CS lines (7-6, 5-4, 3-2, and 2-1). The CS inner abundance is 4×10^{-8} for IRAS05358, IRAS16272, and DR21(OH) while the abundance is lower for NGC6334I(N) (an order of magnitude: 4×10^{-9}) and W43-MM1 (9×10^{-9}). All parameters are given in Table D.1. We have first modeled the CS 11-10 line solely with constant turbulent and infall velocities, but, as for water, adopting a turbulence increasing with the radius (but constant infall) improves the line fitting, specially when including the other CS lines. The resulting V_{turb} profiles are overplotted on Fig. 7 with turbulence inferred from water lines, but should be considered with caution as the CS model is less constrained than water's one due to a significantly lower number of lines involved in the process. The variation of these "two" turbulent velocities is not strictly identical, the obvious difference being a lower turbulence for CS lines. This could be consistent with CS not tracing exactly the same gas than water lines, being located more in the inner part of the envelope where the turbulence is lower: as proposed in Sect. 7.2, water is produced by gas-phase synthesis of H₂O from shocked material in the outflow cavity and CS likely not.

Compared to previous publications, our CS abundances are larger by almost two orders of magnitude for IRAS05358 (Herpin et al. 2009) and DR21(OH) (Richardson et al. 1994), but consistent with Cortes (2011) for W43-MM1. These CS abundances are in agreement with predictions from chemical model (Roberts et al. 2010): the lower CS abundance in the less evolved mid-IR quiet sources, NGC6334I(N) and W43-MM1, might indicate that CS is depleted on the grain mantles in these younger objects. The abundance of CS is dependent on the evaporation of sulfur from the ice mantles by radiation from the central star.

Appendix E: Methanol lines

From the CH₃OH ($v_t = 0$) integrated lines fluxes, corrected from the beam dilution (reference beam is 21.1''), and assuming LTE, we have made the rotational diagrams for all sources (see Fig. E.1) up to $E_{up}/k_B = 440$ K for DR21(OH) and W43-MM1, and up to $E_{up}/k_B = 200$ K for IRAS16272 and IRAS05358. We have estimated the rotational temperature and the total methanol column density, using the partition function from Villanueva et al. (2012). All rotational diagrams can be described by a single temperature, but $\ln(N_{up}/g_{up})$ values are scattered for W43-MM1 and IRAS16272 either because of opacity effects or of non-LTE conditions. Even for our very limited sample of methanol transi-

tions, we have attempted to iteratively correct individual N_{up}/g_{up} values by multiplying by the optical depth correction factor after the method of Goldsmith & Langer (1999). We find that the corrected optical depth is always < 1 , and the correction factors are less than 1%. Taking into account the uncertainties, we note that the rotational temperature possibly increase with the evolutionary sequence assumed in this paper, hence underlining the increasing temperature in the protostellar envelope. Beam-averaged methanol column densities are a few 10^{15} cm⁻² for all sources, except for DR21(OH) where the column density is one order of magnitude larger. The fact that we detect torsionally excited methanol lines ($v=1$) in DR21(OH) and W43-MM1 and that the number of detected CH₃OH lines increases with the source luminosity reveal the role of the IR pumping on the methanol emission (Leurini et al. 2007).

Table A.1. AORs list of Herschel observations for each source.

Transitions	NGC6334I(N)	DR21(OH)	IRAS16272	IRAS05358
o-H ₂ ¹⁸ O 1 ₁₀ -1 ₀₁ ^a	1342205282	1342210764	1342205524	1342205275
o-H ₂ ¹⁷ O 1 ₁₀ -1 ₀₁	1342205279	1342192361	1342191556	1342194488
p-H ₂ ¹⁸ O 2 ₀₂ -1 ₁₁	1342204518	1342195025	1342203167	1342204509
o-H ₂ ¹⁸ O 3 ₁₂ -3 ₀₃	1342206384	1342196427	1342214418	1342206123
p-H ₂ ¹⁸ O 1 ₁₁ -0 ₀₀	1342206383	1342197974/1342194794	1342214417/1342192584	1342206126/1342206124
p-H ₂ ¹⁷ O 1 ₁₁ -0 ₀₀	1342206384	1342196427	1342214418	1342206123
o-H ₂ ¹⁷ O 2 ₁₂ -1 ₀₁	1342214455	1342192569	1342192584	1342203954
o-H ₂ O 1 ₁₀ -1 ₀₁ ^a	1342205282	1342210764	1342205524	1342205275
p-H ₂ O 2 ₁₁ -2 ₀₂	1342205847	1342194574	1342205845	1342194684
p-H ₂ O 5 ₂₄ -4 ₃₁		1342223425		
p-H ₂ O 2 ₀₂ -1 ₁₁	1342204519	1342195026	1342203168	1342204510
o-H ₂ O 3 ₁₂ -3 ₀₃	1342206384	1342196427	1342214418	1342206123
p-H ₂ O 1 ₁₁ -0 ₀₀	1342206383	1342197974/1342194794	1342214419/1342192584	1342206126/1342206124
o-H ₂ O 2 ₂₁ -2 ₁₂	1342214455	1342192569	1342192584	1342203954
o-H ₂ O 2 ₁₂ -1 ₀₁	1342214455	1342192569	1342192584	1342203954

Table B.1. Observed line emission parameters for the detected "by-product" lines toward IRAS05358. v_{LSR} is the Gaussian component peak velocity. Δv are the velocity full width at half-maximum (FWHM) of the narrow, medium and broad components.

Species Line	Freq [GHz]	E_u [K]	$\int T dv$ [K.km/s]	V_{nar} [km/s]	ΔV_{nar} [km/s]	V_{med} [km/s]	ΔV_{med} [km/s]	V_{br} [km/s]	ΔV_{br} [km/s]
CH₃OH									
5 _{1,5} – 4 _{0,4} A ₊ – A ₊	538.57058	49.1	1.3±0.2	-15.7±0.5	3.4±0.2				
6 _{3,4} – 5 _{2,3} A ₊ – A ₊	542.00098	98.5	0.89±0.2	-16.0±0.5	4.0±0.5				
6 _{3,3} – 5 _{2,4} A ₋ – A ₋	542.08194	98.5	0.91±0.2	-16.0±0.5	4.5±0.5				
8 _{1,7} – 7 _{0,7} E	553.14630	104.6	0.6±0.1			-14.2±0.5	6.2±0.9		
12 _{1,11} – 11 _{0,11} E	751.56340	202.1	0.58±0.1			-14.8±0.5	5.2±0.9		
7 _{4,4} – 6 _{3,3} A ₋ – A ₋	974.87674	145.3	1.1±0.2	-16.3±0.3	4.8±0.6				
10 _{2,8} – 9 _{1,9} A ₊ – A ₊	986.09797	165.4	0.6±0.2	-15.3±0.3	3.0±0.5				
5 _{-5,0} – 4 _{-4,1} E	994.21725	158.8	0.7±0.2			-16.0±0.4	5.8±0.8		
¹³CO									
5 – 4	550.92629	79.3	27±4	-16.2±0.5	3.3±0.5	-16.2±0.5	8.5±0.6		
10 – 9	1101.3497	290.8	7±1	-15.9±0.3	3.8±0.3			-14.9±0.3	14.6±0.6
C¹⁸O									
9 – 8	987.5604	237.0	1.0±0.8	-16.3±0.3	4.6±0.5				
10 – 9	1097.16288	289.7	0.4±0.1	-16.0±0.3	3.5±0.3				
CS									
11 – 10	538.6888	155.1	1.2±0.3	-15.7±0.2	3.7±0.3				
H₂O⁺									
1 ₁₁ – 0 ₀₀ J = 3/2 – 1/2	1115.204		-0.5±0.2					-15.1±1.2 ^a	11±3
H₂S									
3 _{0,3} – 2 _{1,2} ^b	993.10825	102.8	1.8±0.3	-15.5±0.3	3.8±0.3				

Notes. ^a in absorption, ^b blended with H₂S 5_{2,3} – 5_{1,4}.

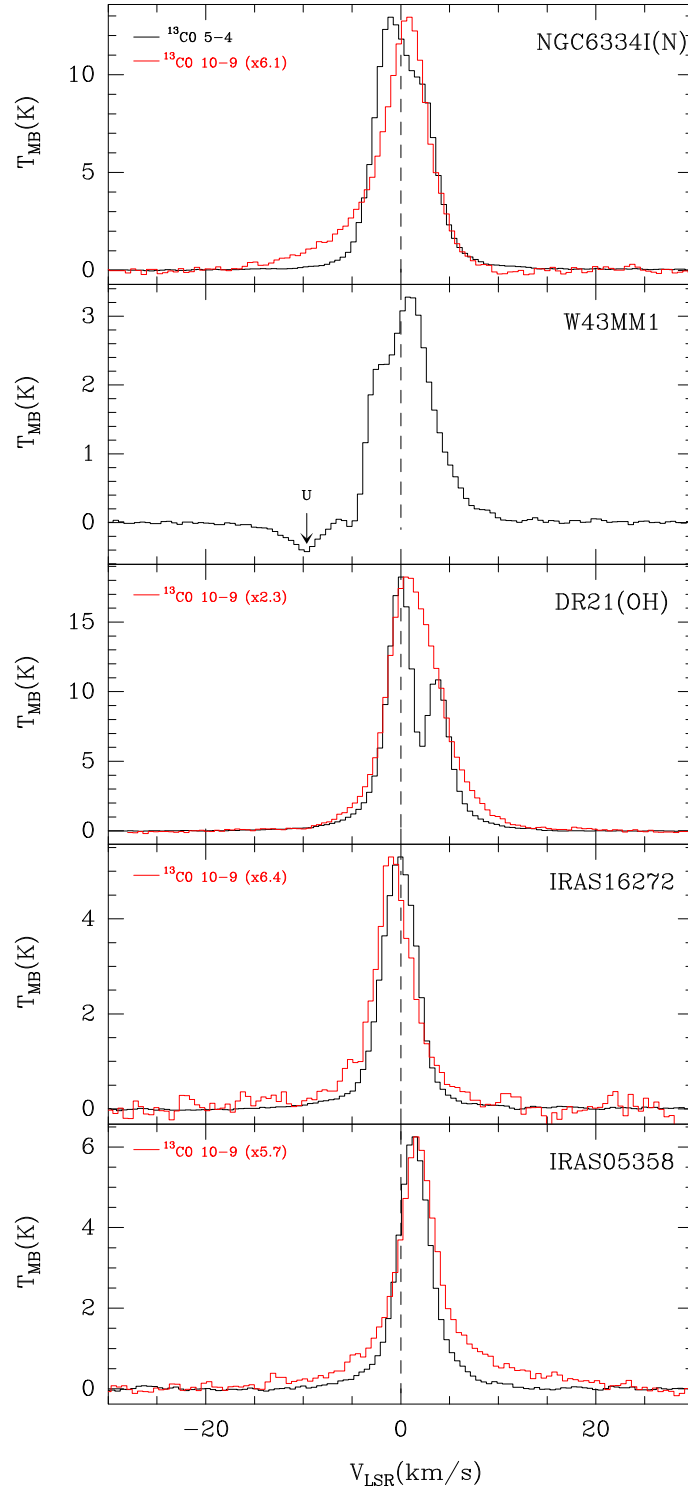


Fig. B.1. HIFI spectra of ^{13}CO $J=5-4$ and $10-9$ lines (respectively in black and red). The spectra have been smoothed to 0.2 km s^{-1} . Vertical dotted lines indicate the V_{LSR} .

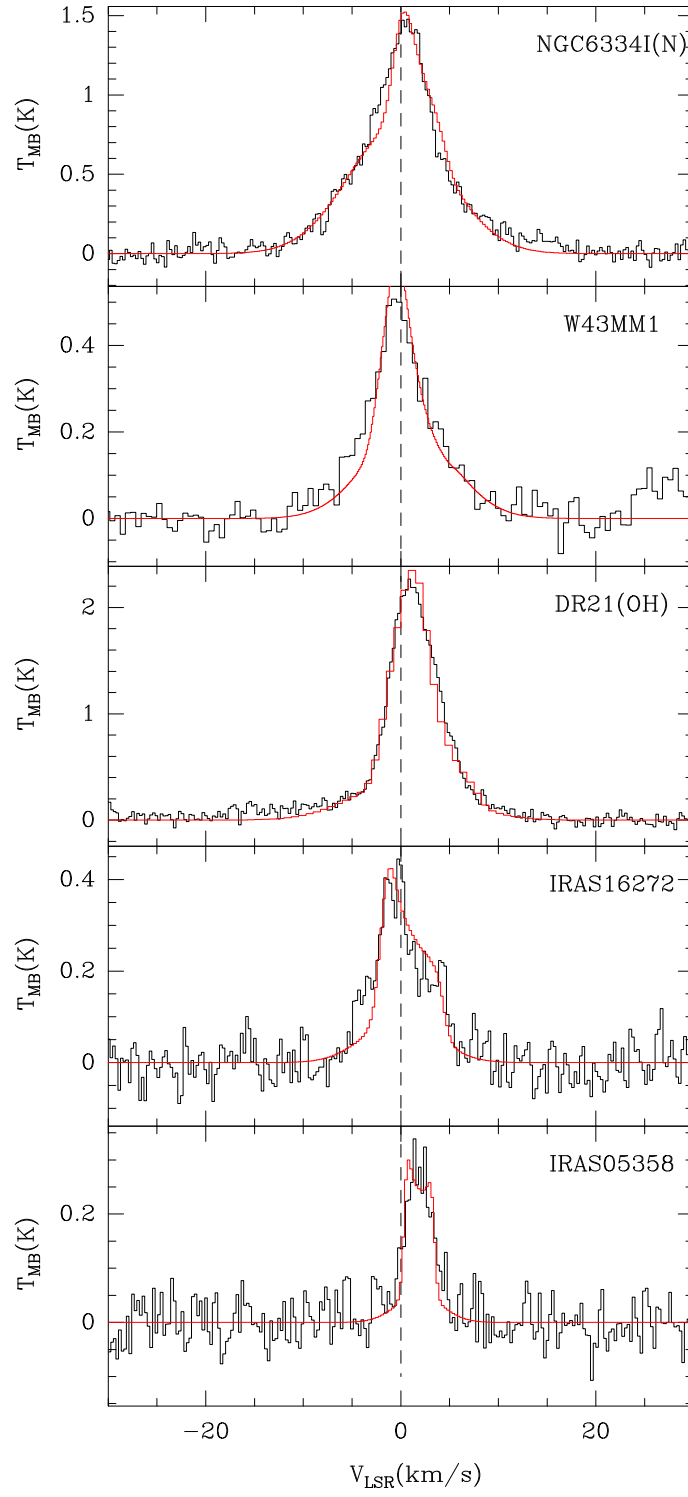


Fig. B.2. HIFI spectra of the CS J=11-10 line. The best-fit model is shown as red over the spectra. Vertical dotted lines indicate the V_{LSR} . The spectra have been smoothed to 0.2 km s^{-1} .

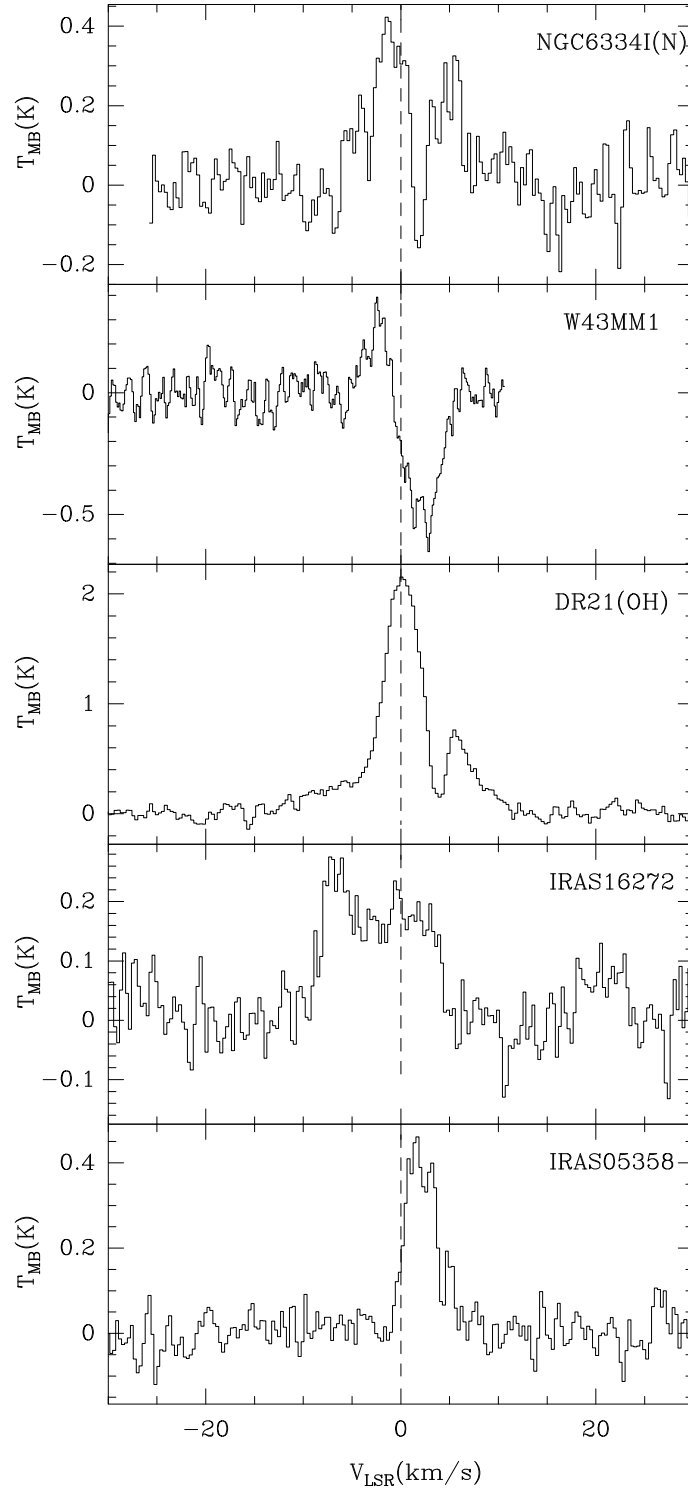


Fig. B.3. HIFI spectra of $\text{H}_2\text{S } 3_{0,3} - 2_{1,2}$ line (blended with the $\text{H}_2\text{S } 3_{0,3} - 2_{1,2}$ line at 993.09701 GHz). The spectra have been smoothed to 0.2 km s^{-1} . Vertical dotted lines indicate the V_{LSR} .

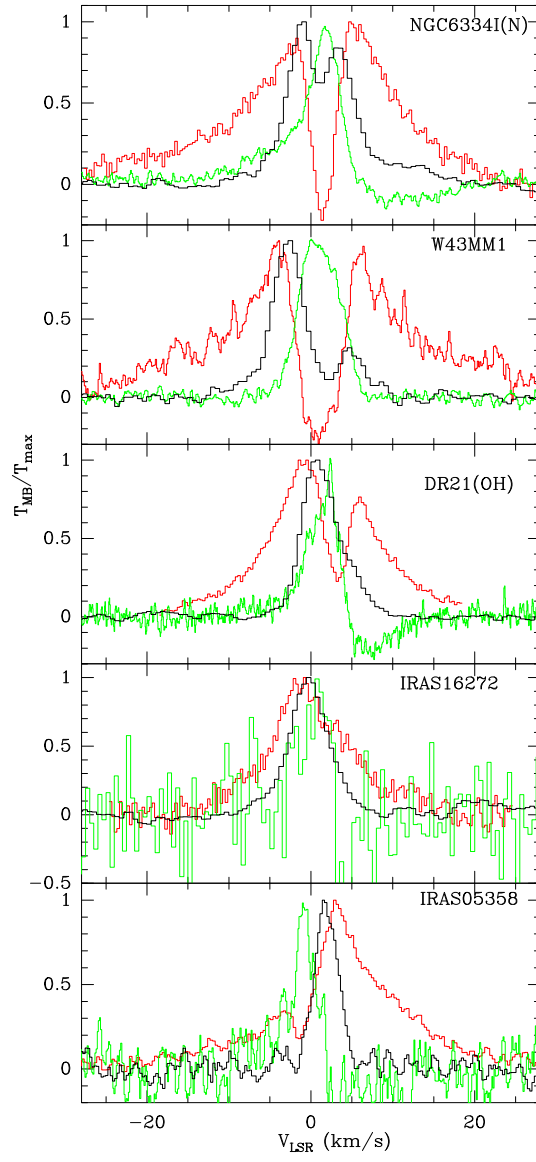


Fig. B.4. HIFI nomalized spectra of $\text{CH}_3\text{OH } 5_{1,5} - 4_{0,4} A_+ - A_+$ line (in black) overplotted on the $\text{p-H}_2\text{O } 2_{02} - 1_{11}$ (red) and $\text{p-H}_2^{18}\text{O } 1_{11} - 0_{00}$ (green and inverted) lines.

Table B.2. Observed line emission parameters for the detected "by-product" lines toward IRAS16272. v_{LSR} is the Gaussian component peak velocity. Δv are the velocity full width at half-maximum (FWHM) of the narrow, medium and broad components.

Species Line	Freq [GHz]	E_u [K]	$\int T d\nu$ [K.km/s]	V_{nar} [km/s]	ΔV_{nar} [km/s]	V_{med} [km/s]	ΔV_{med} [km/s]	V_{br} [km/s]	ΔV_{br} [km/s]
CH₃OH									
5 _{1,5} – 4 _{0,4} A ₊ – A ₊	538.57058	49.1	3.4±0.6			-46.4±0.5	5.7±0.5		
6 _{3,4} – 5 _{2,3} A ₊ – A ₊	542.00098	98.5	1.8±0.4			-46.7±0.5	5.2±0.7		
6 _{3,3} – 5 _{2,4} A ₋ – A ₋	542.08194	98.5	2.0±0.6			-46.6±0.6	5±0.1		
8 _{1,7} – 7 _{0,7} E	553.14630	104.6	1.3±0.2			-47.1±0.6	5.1±0.6		
18 _{2,17} – 18 _{1,18} A ₋ – A ₊	553.57085	434.2	0.4±0.1	-47.6±0.6	3.8±0.9				
12 _{1,11} – 11 _{2,9} E	554.05552	202.1	2.6±0.6	-42.9±0.6	2.9±0.6	-43.7±0.6	8.4±0.6		
12 _{1,11} – 11 _{0,11} E	751.56340	202.1	0.8±0.1	-41.8±0.5	3.8±0.5				
17 _{-3,15} – 17 _{-2,16} E ^b	753.86643	417.7	0.4±0.1	-47.7±0.4	3.5±0.9				
7 _{4,4} – 6 _{3,3} A ₋ – A ₋	974.87674	145.3	0.8±0.2	-47.8±0.3	4.6±0.7				
10 _{2,8} – 9 _{1,9} A ₊ – A ₊	986.09797	165.4	1.3±0.4			-46.6±0.3	6.7±0.8		
5 _{-5,0} – 4 _{-4,1} E	994.21725	158.8	0.5±0.1	-47.2±0.4	3.5±0.5				
9 _{7,3} – 10 _{6,5} E ^b	995.92310	354.2	0.4±0.1	-46.7±0.4	2.6±0.7				
¹³CO									
5 – 4	550.92629	79.3	26±4	-46.3±0.5	4.0±0.5			-47.4±0.5	12.±1
10 – 9	1101.3497	290.8	3.5±0.8	-47.0±0.3	3.4±0.3			-46.8±0.3	10.5±0.9
C¹⁸O									
9 – 8	987.5604	237.0	2.±2			-46.4±0.3	9.9±0.9		
CS									
11 – 10	538.6888	155.1	2.3±0.4			-46±0.1	7.0±1		
H₂O⁺									
1 ₁₁ – 0 ₀₀ J = 3/2 – 1/2	1115.204		-8±1.					-34.5.1±0.5 ^a	23.7±0.7
H₂S									
H ₂ S 3 _{0,3} – 2 _{1,2} ^c	993.10825	102.8	0.9±0.4	-48.6±0.4	3.7±0.7				

Notes. ^a in absorption, ^b band edge, ^c blended with H₂S 5_{2,3} – 5_{1,4}.

Table B.3. Observed line emission parameters for the detected "by-product" lines toward NGC6334I(N). v_{LSR} is the Gaussian component peak velocity. Δv are the velocity full width at half-maximum (FWHM) of the narrow, medium and broad components.

Species Line	Freq [GHz]	E_u [K]	$\int T dv$ [K.km/s]	V_{nar} [km/s]	ΔV_{nar} [km/s]	V_{med} [km/s]	ΔV_{med} [km/s]	V_{br} [km/s]	ΔV_{br} [km/s]
CH₃OH									
5 _{1,5} – 4 _{0,4} A ₊ – A ₊	538.57058	49.1	7.3±1.2			-3.5±0.6	10±1		
15 _{0,15} – 14 _{1,13} E ^a	540.92223	290.7	0.6±0.2			-3.2±0.6	6.9±0.7		
6 _{3,4} – 5 _{2,3} A ₊ – A ₊	542.00098	98.5	5.4±0.4	-3.7±0.5	4.9±0.5				
6 _{3,3} – 5 _{2,4} A ₋ – A ₋	542.08194	98.5	5.2±1.1	-3.8±0.5	4.8±0.6				
8 _{1,7} – 7 _{0,7} E	553.14630	104.6	4.5±0.2			-3.8±0.6	5.1±0.6		
12 _{1,11} – 11 _{0,11} E	751.56340	202.1	14.4±0.4			-6.8±0.5	7.6±0.5	-7.6±0.5	35±1
7 _{4,4} – 6 _{3,3} A ₋ – A ₋	974.87674	145.3	1.6±0.5	-4.2±0.3	4.9±0.5				
10 _{2,8} – 9 _{1,9} A ₊ – A ₊	986.09797	165.4	1.1±0.3	-3.9±0.3	4.0±0.4				
CH₃OCHO									
47 _{6,42} – 46 _{6,41} ^b	551.18200	682.2	0.7±0.4	-7.3±0.5	3.6±0.5				
¹³CO									
5 – 4	550.92629	79.3	85±12			-4.5±0.5	6.3±0.5		
10 – 9	1101.3497	290.8	14±2	-3.7±0.3	4.4±0.3			-6.4±0.3	11.6±0.3
C¹⁸O									
9 – 8	987.5604	237.0	1.7±0.5	-3.6±0.1	2.6±0.3				
10 – 9	1097.16288	289.7	2.7±1.1			-3.7±0.9	7±2		
H₂S									
3 _{0,3} – 2 _{1,2} ^c	993.10825	102.8	1.4±0.4	-5.7±0.4	3.3±0.4				
HDO									
3 _{1,2} – 3 _{0,3} ^a	753.41115	167.6	0.5±0.4	-3.7±0.5	4.1±0.7				
CS									
11 – 10	538.6888	155.1	12.4±1.1	-4.0±0.1	4.5±0.3			-4.7±0.2	13.3±0.6

Notes. ^a band edge, ^b blended with CH₃OCHO 47_{5,42} – 46_{5,41}, ^c blended with H₂S 5_{2,3} – 5_{1,4}.

Table B.4. Observed line emission parameters for the detected "by-product" lines toward W43-MM1. v_{LSR} is the Gaussian component peak velocity. Δv are the velocity full width at half-maximum (FWHM) of the narrow, medium and broad components.

Species Line	Freq [GHz]	E_u [K]	$\int T dv$ [K.km/s]	V_{nar} [km/s]	ΔV_{nar} [km/s]	V_{med} [km/s]	ΔV_{med} [km/s]	V_{br} [km/s]	ΔV_{br} [km/s]
CH₃OH									
5 _{1,5} – 4 _{0,4} A ₊ – A ₊	538.57058	49.1	3.0±1.0			98.0±1	5±1		
6 _{3,4} – 5 _{2,3} A ₊ – A ₊	542.00098	98.5	3.4±0.9			99.3±0.6	6±1		
6 _{3,3} – 5 _{2,4} A _– – A _–	542.08194	98.5	3.0±0.9			99.2±0.6	6±1		
8 _{1,7} – 7 _{0,7} E	553.14630	104.6	2.9±0.2			98.8±0.5	7.1±0.5		
$\nu t = 1$ 5 _{1,5} – 5 _{2,4} A ₊ – A _–	553.20160	359.9	0.6±0.1			100±1	8±3		
$\nu t = 1$ 4 _{1,4} – 4 _{2,3} A ₊ – A _–	553.43748	348.4	0.6±0.1			99.5±0.5	7±1		
18 _{2,17} – 18 _{1,18} A _– – A ₊	553.57085	434.2	0.4±0.1			102.1±0.6	6±1		
12 _{1,11} – 11 _{2,9} E	554.05552	202.1	1.5±0.4			99.5±0.6	8±1		
12 _{1,11} – 11 _{0,11} E	751.56340	202.1	1.6±0.4			104.4±0.5	7.7±0.6		
7 _{4,4} – 6 _{3,3} A _– – A _–	974.87674	145.3	2.8±0.6			97.1±0.3	6.9±0.4		
10 _{2,8} – 9 _{1,9} A ₊ – A ₊	986.09797	165.4	3.1±0.6			98.4±0.3	5.5±0.3	96.7±0.4	13.1±0.3
5 _{–5,0} – 4 _{–4,1} E	994.21725	158.8	0.30±0.07	98.1±0.3	2.6±0.3				
CH₃OCHO									
47 _{6,42} – 46 _{6,41} ^c	551.18200	682.2	0.5±0.1			98.1±0.5	5±1		
¹³CO									
5 – 4	550.92629	79.3	22±5			99.3±0.6	6.5±0.6		
10 – 9 ^b	1101.3497	290.8							
C¹⁸O									
9 – 8	987.5604	237.0	1.7±0.9			99.4±0.2	5.6±0.3		
10 – 9	1097.16288	289.7	0.7±0.1	99.9±0.3	4.5±0.4				
CS									
11 – 10	538.6888	155.1	3.5±0.8	98.3±0.3	2.9±0.9			98.8±0.4	10±1
H₂S									
3 _{0,3} – 2 _{1,2} ^d	993.10825	102.8	-0.9±0.1			98.1±0.5	7±1		
H₂O⁺									
1 ₁₁ – 0 ₀₀ J = 3/2 – 1/2 ^a	1115.204		-8.2±1.2	96.7±0.3	3.2±0.3	100.6±0.3	9.3±0.3		
H₃O⁺									
0(0) – 1(0), 0 [–] – 0 ⁺ ^a	984.70866	54.6	-2.1±0.4			98.0±0.3	7.8±0.5		
HDO									
3 _{0,3} – 2 _{1,2}	995.41150	131.4	0.4±0.7	98.8±0.2	2.7±0.4				

Notes. ^a in absorption, ^b blended with H₂O⁺, ^c blended with CH₃OCHO 47_{5,42} – 46_{5,41}, ^d blended with H₂S 5_{2,3} – 5_{1,4}.

Table B.5. Observed line emission parameters for the detected "by-product" lines toward DR21(OH). v_{LSR} is the Gaussian component peak velocity. Δv are the velocity full width at half-maximum (FWHM) of the narrow, medium and broad components.

Species Line	Freq [GHz]	E_u [K]	$\int T dv$ [K.km/s]	V_{nar} [km/s]	ΔV_{nar} [km/s]	V_{med} [km/s]	ΔV_{med} [km/s]	V_{br} [km/s]	ΔV_{br} [km/s]
CH₃OH									
5 _{1,5} – 4 _{0,4} A ₊ – A ₊	538.57058	49.1	8.5±1.2			-3.3±0.5	5.5±0.7		
6 _{3,4} – 5 _{2,3} A ₊ – A ₊	542.00098	98.5	6.1±1.2			-2.8±0.5	5.9±0.9		
6 _{3,3} – 5 _{2,4} A ₋ – A ₋	542.08194	98.5	6.0±1.			-2.9±0.5	6.1±0.5		
8 _{1,7} – 7 _{0,7} E	553.14630	104.6	3.8±0.2			-3.0±0.3	5.3±0.3		
$vt = 1$ 5 _{1,5} – 5 _{2,4} A ₊ – A ₋	553.20160	359.9	0.4±0.1			-4±1	5±2		
18 _{2,17} – 18 _{1,18} A ₋ – A ₊	553.57085	434.2	0.7±0.2	-3.6±0.5	2.5±0.7			1±1	11±2
12 _{1,11} – 11 _{2,9} E	554.05552	202.1	0.8±0.1			-2.5 ±0.3	5.3±0.5		
12 _{1,11} – 11 _{0,11} E	751.56340	202.1	2.6±0.5			2.3±0.3	6.1±0.4		
11 _{-2,10} – 10 _{-1,10} E	959.34565	179.2	2.4±1.2			-2.8±0.9	6±2		
9 _{-4,6} – 8 _{-3,6} E	959.90049	192.3	3.2±0.7			-2.7±0.4	6.3±0.4		
20 _{-2,19} – 19 _{-2,18} E	970.83461	514.2	0.8±0.2			-2.9±0.4	5.5±0.8		
15 _{3,13} – 14 _{2,12} A ₊ – A ₊	974.67316	328.3	2.4±1.2			-3±1	7±3		
7 _{4,4} – 6 _{3,3} A ₋ – A ₋	974.87674	145.3	3.5±0.6	-3.8±0.3	4.6±0.5				
10 _{2,8} – 9 _{1,9} A ₊ – A ₊	986.09797	165.4	3.4±0.6			-3.0±0.6	5±1		
5 _{-5,0} – 4 _{-4,1} E	994.21725	158.8	6.5±0.07	-3.4±0.3	4.0±0.4			-2.3±0.3	13.8±0.5
CH₃OCH₃									
19 _{7,13} – 19 _{6,12} ^e	740.13792	241.8	2.2±0.1			-4.2±0.5	10±1		
CH₃OCHO									
47 _{6,42} – 46 _{6,41} ^f	551.18200	682.2	2.1±0.5			-3.9±0.4	8.1±0.9		
¹³CO									
5 – 4	550.92629	79.3	89±18	-2.5±0.5	3.1±0.5	-2.5±0.5	9.2±0.6		
10 – 9	1101.3497	290.8	57±12	-3.8±0.3	3.9±0.3	-2.6±0.3	8.1±0.3		
C¹⁸O									
9 – 8	987.5604	237.0	12.1±1.5			-3.1±0.1	5.6±0.1		
10 – 9	1097.16288	289.7	8±2			-3.2±0.7	6±1		
¹³CS									
24 – 23	1107.51176	665.1	1.5±0.4			-5.2±0.3	9.9±0.7		
CS									
11 – 10	538.6888	155.1	13.3±1.1			-3.2±0.2	6.1±0.2		
H₂O⁺									
1 ₁₁ – 0 ₀₀ $J = 3/2 - 1/2^a$	1115.204		-37±7			7.6±0.3	6.9±0.3	2.5±0.3	33.7±0.3
CH⁺									
2 – 1 ^a	1669.28129	120.2	-3.2±0.7	-2.3±0.9	2.6±0.2				
OH⁺									
1 – 0 ^a	971.800		-64±7					1.0±0.5	20.6±0.3
H₂S									
3 _{0,3} – 2 _{1,2} ^g	993.10825	102.8	9±2	-4.3±0.5	4.0±0.4				
H₂CO									
13 _{1,12} – 12 _{1,11}	970.19918	339.0	2.2±0.6			-2.3±0.6	10±1		
HDO									
3 _{0,3} – 2 _{1,2}	995.41150	131.4	4.0±0.7					-1.3±0.3	11.4±0.4
3 _{1,2} – 3 _{0,3} ^c	753.41115	167.6	1.4±0.2			-1.5±0.3	7.2±0.5		
OS¹⁸O									
20 _{8,13} – 19 _{7,12} ^d	1108.60656	352.3	1.4±0.3			-3.4±0.4	7.6±0.9		
SO₂									
10 _{6,4} – 9 _{5,5}	753.06035	138.8	0.9±0.4			-0.9±0.3	5.3±0.5		
13 _{9,5} – 12 _{8,4} ^c	1113.50582	281.9	0.5±0.4			-0.3±0.3	5±1		
12 _{9,3} – 11 _{8,4}	1094.32950	269.9	3.5±1.	2.7±0.4	4.0±0.6	-7.6±0.3	10.0±0.6		
11 _{8,4} – 10 _{7,3}	974.60251	217.4	1.4±1.0			0±1	5±2		
12 _{8,4} – 11 _{7,5}	993.76628	228.5	1.8±1.0			-1.8±0.4	8.9±0.9		
16 _{7,9} – 15 _{6,10}	969.22389	245.1	0.9±0.2			-0.4±0.4	5.8±0.6		
20 _{14,6} – 21 _{13,9}	956.82941	670.3	0.5±0.2	-2.5±0.4	2.8±0.7				
31 _{1,31} – 30 _{0,30} ^c	554.21278	431.5	1.1±0.6			1.3±0.5	9±2		
³⁴SO									
26 ₂₆ – 25 ₂₅	1095.06010	723.3	0.6±0.4			-3.3±0.6	6±1		

Notes. ^a in absorption, ^c band edge, ^d blended with OS¹⁸O 20_{8,12} – 19_{7,13}, ^e blended with CH₃OCH₃ 19_{7,12} – 19_{6,13}, ^f blended with CH₃OCHO 47_{5,42} – 46_{5,41}, ^g blended with H₂S 5_{2,3} – 5_{1,4}.

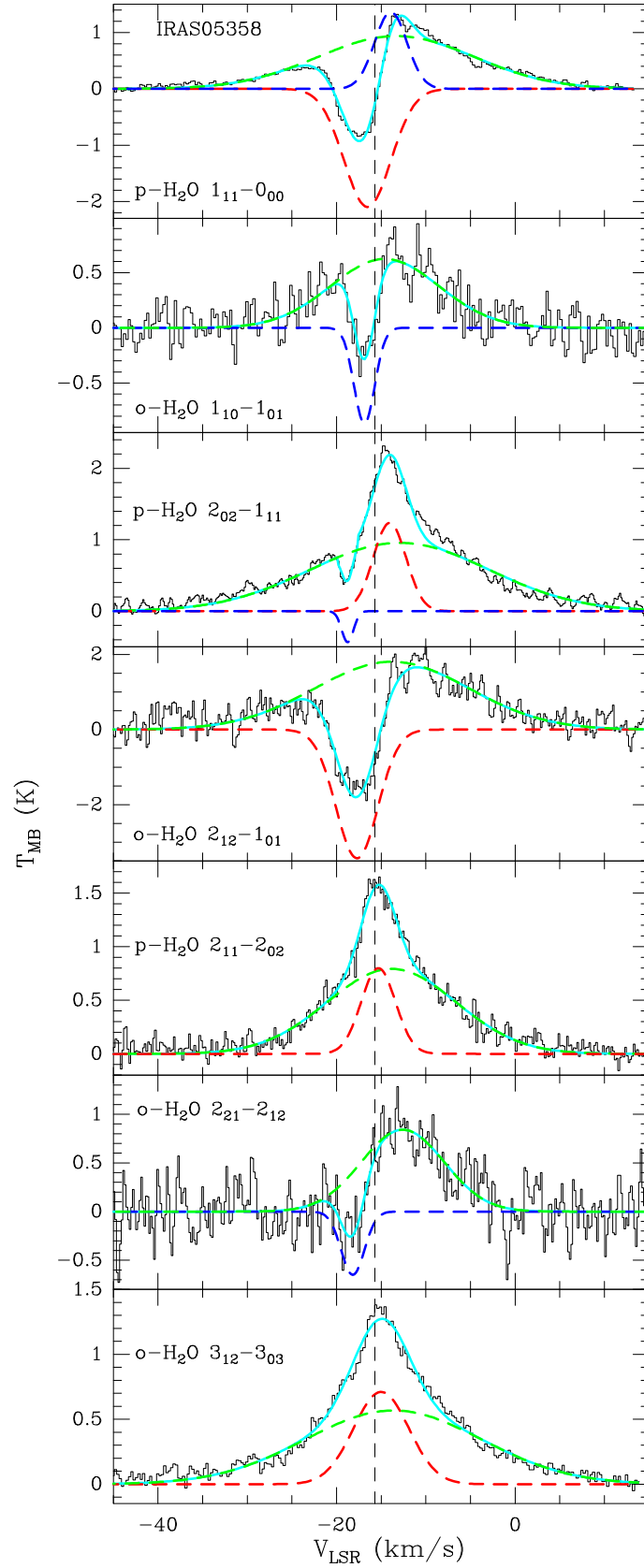


Fig. C.1. Gaussian fit components (red, blue, and green) for H_2^{16}O lines in IRAS05358. The light blue curve stands for the total fit.

Table D.1. CS parameters derived from model. The turbulent and infall velocities are the nominal constant values for modeling the CS 11-10 line solely.

Object	χ_{in} 10^{-8}	χ_{out} 10^{-8}	V_{turb} [km s $^{-1}$]	V_{inf} [km s $^{-1}$]	\dot{M}_{acc} [M $_{\odot}$.yr $^{-1}$]
NGC6334I(N)	0.4	0.1	1.5	-2.4	2.5×10^{-4}
W43-MM1	0.9	0.03	2.4	-1.9	2×10^{-2}
DR21(OH)	4.0	3.0	1.6	-2.0	6.6×10^{-5}
IRAS16272	3.5	0.4	1.6	-0.8	3.7×10^{-5}
IRAS05358	4.0	0.7	0.8	0.0	

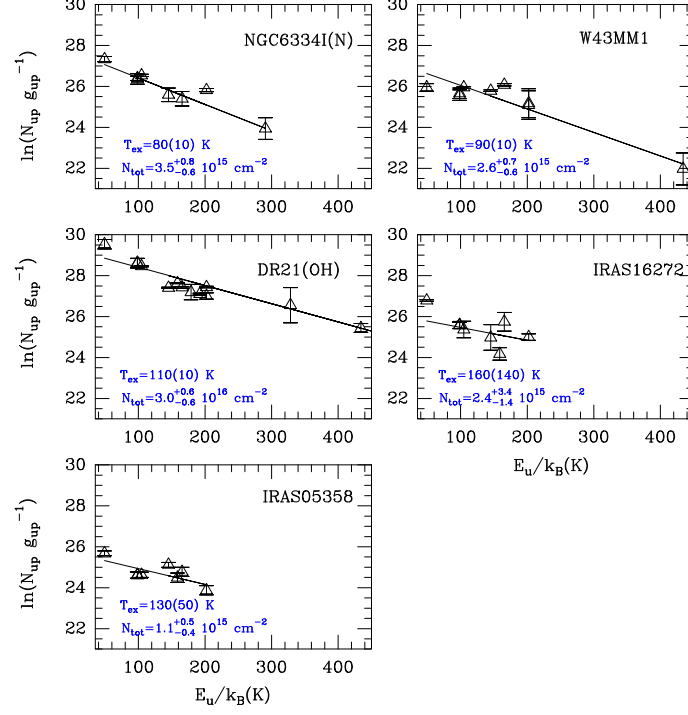


Fig. E.1. Rotational diagrams for methanol lines ($v_t = 0$). Sources are ordered following the evolutionary sequence.